Bulk Compositional Influence on Diverse Metapelitic Mineral Assemblages in the Whetstone Lake Area, Ontario

Jacob B. Forshaw[1,2,*] and David R.M. Pattison[1]

[1]Department of Geoscience, University of Calgary, 2500 University Drive, Calgary, Canada T2N 1NV
[2]Institut für Geologie, Universität Bern, Baltzerstrasse 1 + 3, 3012 Bern, Switzerland

*Corresponding author. E-mail: jacob.forshaw@geo.unibe.ch

Abstract

Understanding the interplay between bulk composition and metamorphic grade underpins our interpretations of metamorphism in orogenic belts. The focus of this study is the regional garnet–staurolite–kyanite–sillimanite metamorphic sequence of the Whetstone Lake area, southeastern Ontario. In the kyanite and lower sillimanite zones of this area, there is exceptional diversity in metapelitic mineral assemblages that cannot be accounted for by differences in metamorphic grade. We present a data set of petrographic observations, phase proportions, whole-rock geochemical compositions, and mineral compositions, from thirty-two samples that encapsulate the range of assemblages found in these zones. Differences in bulk composition are the primary control on mineral assemblage development. Whole-rock $X_{Mg} = $ molar $MgO/(MgO + FeO)$ and $X_{Fe^{3+}} = $ molar $2 \times Fe_2O_3/(2 \times Fe_2O_3 + FeO)$ exert the greatest control on the observed mineral assemblages, whilst variation in MnO, K_2O, and Al_2O_3 have a secondary influence. We use a set of *quality factors* (Duesterhoeft & Lanari, 2020) to test the ability of thermodynamic models to reproduce the observed mineral assemblages, modal abundances, and mineral compositions in the diverse bulk compositions at Whetstone Lake. Eight samples were selected for phase equilibrium modelling, for which two bulk compositions were calculated for each sample: (1) a whole-rock bulk composition based on an X-ray fluorescence analysis and (2) a carefully considered local bulk composition based on combining mineral proportions with representative mineral compositions, as obtained from a single thin section. Our modelling uses thermodynamic data set 6.2 (Holland & Powell, 2011) and the solution models of White *et al.* (2014a, 2014b) that incorporate several Fe^{3+} end members needed to model the natural data. Modelling in both types of bulk composition broadly predicted mineral assemblages that match those observed. In addition, predicted mineral assemblage fields overlap within uncertainty between 620°C and 675°C and between 6.5 and 7.5 kbar, consistent with the limited range of grade represented by the natural rocks. Predicted modal abundances better match those observed when phase diagrams are constructed using local bulk compositions compared to whole-rock bulk compositions. Despite the acceptable agreement between predicted and observed mineral assemblages, consistent discrepancies are found between predicted and observed mineral compositions. These include overestimation of X^*_{Mg} in garnet, staurolite, and cordierite, overestimation of Ti in staurolite and biotite, underestimation of Si in biotite, and overestimation of Al and underestimation of Fe^{3+}, Fe^{2+}, and Mg in muscovite. The Whetstone Lake suite of this study will be useful to test the predictive capability of future thermodynamic models.

Key words: metapelite; metamorphism; phase equilibria; phase equilibrium modelling; rock composition; oxidation state

INTRODUCTION

In his pioneering work, George Barrow documented a sequence of index mineral-based metamorphic zones (chlorite–biotite–garnet–staurolite–kyanite–sillimanite) across south-eastern Scotland (Barrow, 1912, 1893). Since Barrow's study, other sequences of metapelitic minerals have been observed in orogenic belts worldwide. The order in which metamorphic mineral assemblages develop varies systematically with pressure and temperature (P–T), in turn providing a means of distinguishing between different P–T conditions of metamorphism (Miyashiro, 1961; Hietanen, 1967; Carmichael, 1978; Pattison & Tracy, 1991). The other major factor that exerts a primary influence on the development of metamorphic mineral assemblages is bulk composition (Eskola, 1915; Chinner, 1960; Hounslow & Moore, 1967; Atherton & Brotherton, 1972; Guidotti *et al.*, 1975). Both factors combine to control

a metamorphic rock's mineral assemblage, mineral proportions, and mineral compositions (Spear, 1993). In order to accurately determine the P–T conditions under which metamorphic mineral assemblages develop, it is, therefore, necessary to understand the interplay between bulk composition and metamorphic grade, a problem which has lain at the heart of metamorphic petrology since its inception over a century ago (Goldschmidt, 1911; Eskola, 1914).

Sequences of metapelitic minerals in the rock record range from those where bulk composition are relatively constant across metamorphic grade to those where bulk composition varies considerably within a single metamorphic zone. There are several localities where whole-rock geochemical studies have found minimal variation in compositions across grade, such that variations in mineral assemblages and mineral compositions can be ascribed to different P–T conditions (Shaw, 1956; Vidale, 1974;

Atherton & Brotherton, 1982; Munksgaard, 1988; Moss *et al.*, 1996; Cesare, 1999; Pattison & Vogl, 2005; Pattison & Debuhr, 2015; Pattison & Goldsmith, 2022). Using a database of 5729 major element whole-rock analyses from the literature, we have shown that whilst pelites worldwide show a strong clustering of analyses on the AFM diagram of Thompson (1957), a significant number of pelite compositions lie outside this main cluster (fig. 2A of Forshaw & Pattison, 2023). This variability can lead to the other extreme in which mineral assemblages vary widely over a small range of grade because of differences in bulk composition. For example, Guidotti *et al.* (1975) demonstrated that the wide variety of assemblages in the upper staurolite and lower sillimanite zones of west-central Maine, USA, result from differences in whole-rock Al, Fe, and Mg (fig. 3 of that paper). Chinner (1960) determined that different mineral assemblages from the kyanite and sillimanite zones of Glen Clova, Scotland, result from varying ferric/ferrous iron ratios between layers. Hudson & Harte (1985) showed the importance of K_2O content on the development of mineral assemblages in the Buchan region, Scotland.

This contribution is concerned with metapelitic rocks of the Whetstone Lake area, southeastern Ontario, which is exceptional in terms of the diversity of assemblages in a limited range of grade. Carmichael (1970) originally highlighted the bulk compositional variation present at Whetstone Lake through the plotting of mineral assemblages on an AFM diagram (figs. 6, 10 and 14 of Carmichael, 1970). This study builds upon Carmichael's (1970) work by showing that the bulk compositional variability is not only restricted to variations in X^*_{Mg} (MgO / (MgO + FeO) in moles), but also involves differences in K_2O, MnO, and $X_{Fe^{3+}}$ ($2 \times Fe_2O_3 / (2 \times Fe_2O_3 + FeO)$ in moles). Whetstone Lake, therefore, provides a natural laboratory for studying the influence of bulk compositional variation on mineral assemblage development, where there is relatively little variation in P–T conditions.

In this paper, we present a data set of petrographic observations, mineral assemblages, phase proportions, bulk compositions, and mineral compositions from the diverse range of metapelitic mineral assemblages in the kyanite and lower sillimanite zones of Whetstone Lake. We first demonstrate how this bulk compositional variability influences the observed mineral assemblages, proportions, and compositions. We then conduct phase equilibrium modelling to test how well current thermodynamic data sets and solution models predict mineral assemblages, modes, and compositions from such a wide range of bulk compositions. Part of this testing involves the application of *quality factors* (Duesterhoeft & Lanari, 2020) that quantify the degree of mismatch between prediction and observation.

GEOLOGICAL BACKGROUND

The Grenville Province is a complex orogenic belt comprising various Precambrian-aged deformed and metamorphosed rocks (Fig. 1a; Easton, 1992; Hynes & Rivers, 2010). In south-eastern Ontario, the Grenville Province is subdivided into the Central Gneiss Belt (CGB), the Central Metasedimentary Belt (CMB), and the Frontenac terrane (Fig. 1b; Easton, 1992; McCarron *et al.*, 2014). The Whetstone Lake area lies within the Elzevir Terrane which forms part of the Central Metasedimentary Belt (Fig. 1).

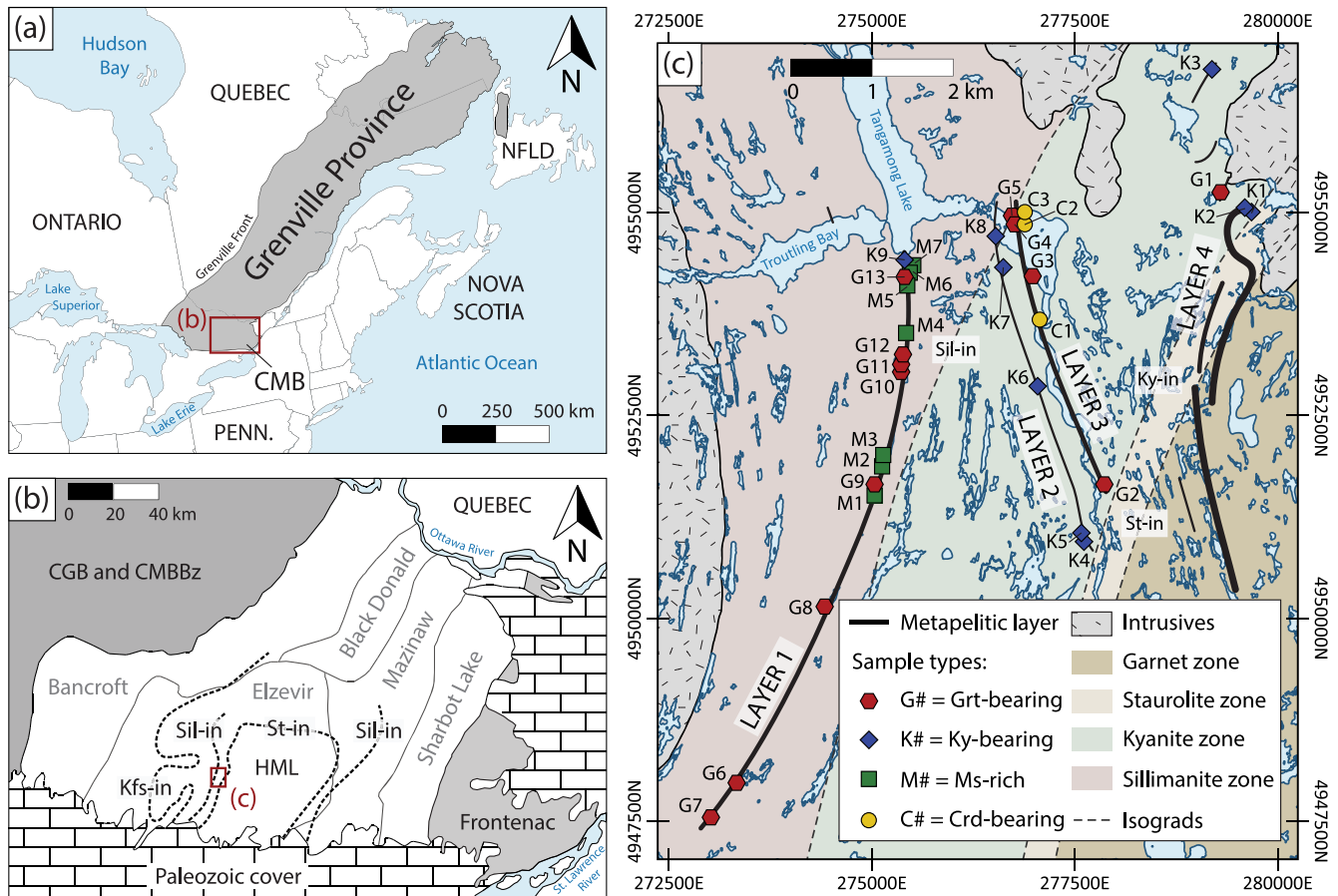### Central Metasedimentary Belt
Previous P–T estimates

The CMB is a major Mesoproterozoic accumulation of supracrustal rocks invaded by compositionally diverse plutonic rocks that were metamorphosed at grades varying from greenschist to granulite facies (Easton, 1992). Greenschist facies rocks are found in the 'Hastings Metamorphic Low', with metamorphic grade increasing to the east, west, and north (Fig. 1b; Anovitz & Essene, 1990; Carmichael, 1970, 1967; Duesterhoeft *et al.*, 2021; Dunn *et al.*, 2019; Ford, 2002; Hounslow & Moore, 1967; Lal & Moorhouse, 1969; McCarron *et al.*, 2014; Rathmell *et al.*, 1999). Several authors have documented the peak P–T conditions of the Central Metasedimentary Belt during the Grenvillian Orogeny and compared these with peak P–T estimates for the adjacent Central Gneiss Belt and Frontenac Terrane (Fig. 1b). Chesworth (1971) classified the Central Metasedimentary Belt as part of the low-pressure intermediate facies series of Miyashiro (1961), and contrasted it with the relatively lower pressure andalusite–sillimanite facies series of the Frontenac Terrane, and the relatively higher pressure kyanite–sillimanite facies series of the Central Gneiss Belt. Anovitz & Essene (1990) compiled a map of aluminosilicates from across southeastern Ontario to delineate broad variations in pressure; these variations were augmented by quantitative thermobarometry using a range of published thermometers and barometers. Anovitz & Essene (1990) estimated P–T conditions of 4 to 8 kbar and 400°C to 650°C across the Central Metasedimentary Belt. Further compilations of thermobarometric data by Streepey *et al.* (1997) and Rathmell *et al.* (1999) returned similar P–T estimates.

Only two published studies have investigated the P–T history of the CMB using phase equilibrium modelling. McCarron *et al.* (2014) modelled metapelitic lithologies of the Mazinaw Terrane, on the eastern side of the 'Hastings Metamorphic Low' (Fig. 1b), using thermodynamic data set 5.5 (Holland & Powell, 1998); they constrained the peak P–T conditions of metamorphism from across their St–Ky–Sil sequence to between 3.5 and 7.9 kbar and 540°C and 715°C (McCarron *et al.*, 2014). Duesterhoeft *et al.* (2021) modelled metasedimentary lithologies of the Elzevir and Bancroft Terranes using the thermodynamic database JUN92 (de Capitani & Petrakakis, 2010), which is based on the thermodynamic data set from Berman (1988); they constrained the peak P–T conditions of metamorphism in the Bancroft Terrane to 10 kbar and 780°C, and peak P–T conditions in the Elzevir Terrane to 9 kbar and 520°C. Samples from the Elzevir Terrane studied in Duesterhoeft *et al.* (2021) were collected from approximately 40 km north of the Whetstone Lake area, close to the K-feldspar-in isograd of Carmichael *et al.* (1978; Fig. 1b). To our knowledge, there are no published studies from the Whetstone Lake region using either phase equilibrium modelling or conventional thermobarometry to assess the *P–T* conditions of metamorphism.

Timing of metamorphism

The Grenville Orogeny encompasses a series of tectonic events grouped into two distinct age categories (Easton, 1992; Rivers, 2008), the Elzevirian Orogeny (~ 1.3–1.2 Ga) and the Ottawan Orogeny (~ 1.1–1.0 Ga). The CMB is interpreted to have been subjected to both events (Easton, 1992; Rivers, 2008; Dunn *et al.*, 2019). There are relatively few geochronological dates from the Elzevir Terrane within which the Whetstone Lake area resides. The emplacement of intrusions in the Elzevir Terrane has been dated at 1280 to 1240 Ma by U–Pb geochronology of zircon (Lumbers *et al.*, 1990). Metamorphism of the Elzevir Terrane has been dated using U–Pb geochronology of sphene and rutile (Mezger *et al.*, 1993). An older rutile age of 1240 Ma is thought to be the result of contact metamorphism associated with the intrusions, whilst younger sphene ages of 1061 to 1012 Ma are interpreted to date the regional metamorphism (Mezger *et al.*, 1993). Uplift of the Elzevir Terrane

Fig. 1. (a) The Grenville Province of Canada and outline of the Central Metasedimentary Belt (CMB). Modified after Hynes & Rivers (2010). (b) Lithotectonic terranes of the CMB: Bancroft, Elzevir, Black Donald, Mazinaw, Sharbot Lake, and Frontenac Terranes. CGB, Central Gneiss Belt; CMBBz, Central Metasedimentary Belt Boundary zone; HML, hastings metamorphic low. Modified after Easton (1992) and McCarron et al. (2014). Isograds after Carmichael et al. (1978). (c) Regional index mineral isograds of the Whetstone Lake area, Ontario, Canada after Forshaw (2021); Figure S1 provides full mineral assemblages). Simplified geology after Carmichael (1970, 1967), Laakso (1968), and Lumbers & Vertolli (2000a, 2000b). Metapelitic layers shown as black lines. Sample localities used in this study shown by the coloured hexagons, diamonds, squares, and circles.

has been constrained to between 1006 and 1026 Ma by $^{40}Ar/^{39}Ar$ hornblende cooling ages (Cosca et al., 1992). Metamorphism of the Mazinaw Terrane, on the eastern side of the 'Hastings Metamorphic Low' (Fig. 1b), has been dated at 976 ± 4 Ma by LA-ICP-MS U–Pb geochronology of monazite (McCarron et al., 2014). Uplift of the Mazinaw Terrane has been constrained to between 919 and 942 Ma by $^{40}Ar/^{39}Ar$ hornblende cooling ages (Cosca et al., 1992). Metamorphism of the Central Metasedimentary Belt boundary zone and Bancroft Terrane, to the north of the 'Hastings Metamorphic Low' (Fig. 1b), has been constrained to 1020 to 1120 Ma by EPMA U–Th–Pb geochronology of monazite (Markley et al., 2018). Uplift of the Central Metasedimentary Belt boundary zone and Bancroft Terrane has been constrained to between 972 and 1010 Ma by $^{40}Ar/^{39}Ar$ hornblende cooling ages (Cosca et al., 1992).

Whetstone Lake area

The Whetstone Lake area is situated within the Belmont Domain of the Elzevir Terrane on the western side of 'Hastings Metamorphic Low' (HML, Fig. 1b; Easton, 1992). The bedrock comprises a succession of Precambrian metasedimentary and metavolcanic strata (Laakso, 1968) that form part of the Mayo group. A detailed account of metamorphic studies in the Whetstone Lake area and its immediate surroundings is provided in Supplemental Material. This study focuses on the thin bands of metamorphosed aluminous clastic sedimentary strata in the area (Fig. 1c), as was

done by Carmichael (1970, 1967). For simplicity, these are referred to as metapelites, although the degree to which they are truly metapelitic is discussed later in the paper. Although these rocks are not abundant, they are widely distributed over the region, and thus contain a range of mineral assemblages that allow changes in metamorphic grade to be identified (Fig. 1c). Grade increases from garnet zone in the south-east through staurolite and kyanite zones into a sillimanite zone in the north-west (Carmichael, 1970).

Metapelitic mineral assemblages were grouped into layers based on the geographic location of samples. There are four major metapelitic layers, named numerically, with the number increasing from west to east (Fig. 1c). Within each layer, there can be significant differences in the mineral assemblages between bands of rock at the scale of an outcrop. Layer one is the most continuous in terms of outcrop and lies in the sillimanite zone, extending south-southwest from Tangamong Lake (Fig. 1c). Layers two and three crop out on the western edge of Whetstone Lake and extend south-southeast, transecting the kyanite zone (Fig. 1c). Layer four, which is discontinuous, has a roughly north–south trend and transects the garnet, staurolite, and kyanite zones (Fig. 1c).

METHODS

Metapelitic samples from across the Whetstone Lake area were used to construct a metamorphic isograd map (Figure S1;

Forshaw, 2021). The wide variety of mineral assemblages across the region made defining isograds, and in turn the relative direction of increasing metamorphic grade, difficult. Carmichael (1970) overcame this issue by plotting 'reaction isograds' which filtered for bulk compositional differences. Here, metamorphic isograds represent the first appearance of an index mineral in rocks of broadly pelitic composition rather than the reaction isograds of Carmichael (1970). The difference between these approaches is discussed in the Supplementary Material. The position of the index mineral isograds of Forshaw (2021) is negligibly different in location to the reaction isograds of Carmichael (1970).

This study focuses on samples from the kyanite and lower sillimanite zones because the maximum diversity of mineral assemblages is found in these zones (Fig. 1c). Thirty-two samples encompassing the range of assemblages found in these zones were chosen for further analyses of whole-rock geochemistry, mineral proportions, and mineral compositions (Fig. 1c). Table S1 lists the sample number, geographic coordinates, metamorphic zone, mineral assemblage, and the types of analyses performed for the 32 samples. Mineral abbreviations are after Warr (2021).

Whole-rock analysis

Whole-rock chemical analyses were obtained for 23 samples which exhibited little to no retrogression. Analysed rock was taken from close to where thin sections were cut, and any weathered exterior surfaces were removed using a rock saw. Between 0.2 and 1 kg of rock were crushed for each sample for whole-rock analysis. Major element concentrations were determined by conventional X-ray fluorescence (XRF) at Activation Laboratories Ltd. (Ancaster, Ontario; total Fe reported as Fe_2O_3). Detection limits for major elements were between 0.001 and 0.01 wt.%. FeO was measured by fluorine titration using a modified Wilson (1955) method at Activation Laboratories, from which Fe_2O_3 was obtained by difference. The detection limit for FeO was 0.1 wt.%. Whole-rock compositions, detection limits, standards, and duplicate analyses are listed in Tables S2 and S3.

Mineral proportions

Mineral proportions were calculated using a combination of two procedures. High-resolution scans of thin sections (27 × 46 mm) were point-counted using the program JMicroVision (Roduit, 2020), in which 500 points were randomly distributed across the images (e.g. Palin et al., 2016; Forshaw et al., 2019). For fine-grained rocks, where matrix minerals (e.g. quartz, plagioclase, and muscovite) could not be separated on slidescans, the matrix was point-counted as a single entity. The same was done for inclusion-rich porphyroblasts (e.g. cordierite and plagioclase), where it was difficult to distinguish inclusions from their hosts. To separate matrix minerals from each other and inclusions from their porphyroblasts, we undertook X-ray compositional mapping using a Bruker energy dispersive spectrometer (EDS) on a JEOL JXA-8200 electron probe micro-analyser (EPMA) at the University of Calgary. Backscattered electron images and element maps of representative areas of matrix and inclusion-rich porphyroblasts were examined using a combination of point counting and colour intensity thresholding to calculate percentages of matrix minerals and porphyroblast inclusions. By combining the modal abundances from EDS maps with those determined from thin section scans, we calculated mineral modal abundances for all samples (Table S4; Fig. 2). Uncertainties on modal abundance estimates were calculated according to Howarth (1998).

Opaque mineral identification

We first attempted to identify opaque minerals using reflected light optical microscopy. However, due to their small size (< 100 μm) and common alteration this proved difficult. We, therefore, used backscattered electron (BSE) images from EPMA to elucidate different types of opaques and their micron-scale features (e.g. lamellae and alteration). Ilmenite and titanohematite exhibit various stages of alteration to leucoxene, a finely crystallized rutile–pseudorutile aggregate formed from the alteration of ilmenite (Temple, 1966; Grey & Reid, 1975; Mücke & Chaudhuri, 1991; Deer et al., 2013). Leucoxene was distinguished from crystalline rutile through its opaque appearance in transmitted light optical microscopy.

Mineral compositions

Mineral compositional analysis was performed on 25 of the 32 samples using wavelength dispersive spectrometry (WDS) and the Probe for Windows Software on a JEOL JXA-8200 EPMA at the University of Calgary. Analyses were conducted on carbon coated, polished thin sections at 15 kV, using a 20-nA beam, and a range of natural and synthetic standards (listed in Table S5). Biotite, muscovite, and chlorite were analysed using a 10-μm beam, plagioclase, garnet, staurolite, cordierite, orthoamphibole, and aluminosilicates with a 5-μm beam, and Fe–oxides with a focussed beam. The Armstrong/Love-Scott $\varphi(\rho z)$ matrix correction with Henke mass adsorption coefficients was automatically applied to all analyses (Armstrong, 1988). Element-distribution maps for Fe, Mg, Ca, and Mn in garnet were obtained using WDS stage scans at 20 kV and 100 nA, with a focussed beam, dwell time of 25 to 50 ms, and step size of 1 to 5 μm. Fig. S3 shows plane-polarised light photomicrographs and X-ray intensity maps of garnet from all samples in which it was mapped.

Between 5 and 40 WDS spot analyses were collected for every mineral in each thin section, the low end for minerals that are in low modal abundance and show evidence for retrogression. Line profiles were taken of porphyroblastic phases, whilst individual spots were chosen randomly from different parts of the thin section for matrix phases. For homogeneous minerals, mean and standard deviation were calculated from all acceptable spot analyses in each sample. Representative core, middle, and rim analyses for garnet were selected from line scans to capture compositional zonation.

EPMA-derived mineral compositional analyses (in wt.% oxide) were converted to molecular mineral formulae using the number of oxygen equivalents per formula unit indicated in brackets for each of the following minerals: plagioclase (8), muscovite (22), chlorite (14), garnet (12), staurolite (46), aluminosilicate (5), cordierite (18), orthoamphibole (23), ilmenite–titanohematite (3), and magnetite (4). Biotite was converted using a 22-oxygen +Ti cation recalculation, as suggested by Waters & Charnley (2002).

Ferric iron was considered as follows. All iron in the aluminosilicates is assumed to be Fe^{3+} (Deer et al., 2013). Cordierite contains an insignificant amount of Fe^{3+} (Geiger et al., 2000), and therefore, it was not considered. The proportion of Fe^{3+} in ilmenite, titanohematite, magnetite, and garnet was determined using the charge-balancing method of Droop (1987). Concerning the latter, measurements of Fe^{3+} in garnet from metapelites indicate that there is negligible Fe^{3+}, and therefore, estimated Fe^{3+} may be a result of analytical error in the other elements, especially Si and Al that are most abundant (Dyar et al., 2012, 2002; Quinn et al., 2016). Nevertheless, to maintain consistency between our natural data and the White et al. (2014a) solution models
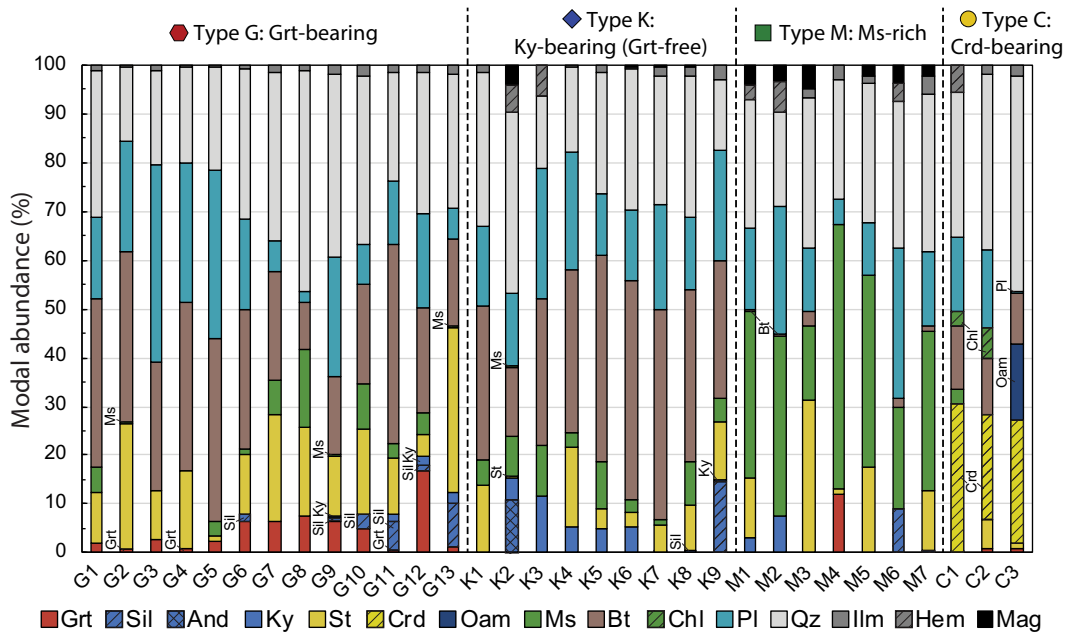
Fig. 2. Modal abundances for the 32 samples examined in this study.

used in thermodynamic predictions discussed below, an estimate of Fe^{3+} in garnet was required. Fe^{3+} contents calculated using the method of Droop (1987) were, therefore, screened and only included if $X_{Fe^{3+}}$ $(2 \times Fe_2O_3 / (2 \times Fe_2O_3 + FeO) = Fe^{3+} / (Fe^{3+} + Fe^{2+})$ in moles) was less than 0.05. For chlorite, staurolite, muscovite, and biotite, $X_{Fe^{3+}}$ was estimated from the study of Forshaw & Pattison (2021), as follows. For biotite, an $X_{Fe^{3+}}$ of 0.11, 0.13, and 0.19 was used for Ilm-bearing, Mag-bearing ($\pm$Ilm), and Hem-bearing ($\pm$Mag $\pm$ Ilm) assemblages respectively. For muscovite, an $X_{Fe^{3+}}$ of 0.49, 0.67, and 0.62 was used for Ilm-bearing, Mag-bearing ($\pm$Ilm), and Hem-bearing ($\pm$Mag $\pm$ Ilm) assemblages respectively. For chlorite and staurolite, uniform average values of 0.08 and 0.07 are assumed irrespective of the type of Fe–oxide, because there were too few analyses in the database of Forshaw & Pattison (2021) to distinguish $X_{Fe^{3+}}$ in these minerals as a function of Fe–oxide type. For orthoamphibole, only present in one sample, an $X_{Fe^{3+}}$ of 0.28 was estimated using the constraints from Hawthorne et al. (2012). Tables S6 to 18 show the weight % oxide analyses and cations per formula unit for each mineral.

SAMPLE CLASSIFICATION

Categorising the wide range of mineral assemblages, modal abundances, and mineral compositions in metapelites from the kyanite and lower sillimanite zones at Whetstone Lake is difficult. Categorization by metamorphic grade was rejected because the diversity of assemblages within the two zones implies that bulk composition exerts more influence on mineral development than metamorphic grade. A second approach would be to classify rocks according to their stratigraphic formation. Whilst studies of other areas have successfully used this approach (e.g. McLellan, 1985; Boger et al., 2012), at Whetstone Lake metasedimentary rocks have not been divided into formations, the four metapelitic layers described above are discontinuous along strike (Lumbers & Vertolli, 2000a), and individual outcrops within the four layers occasionally contain different mineral assemblages. A third approach would be to classify samples based on the presence or absence of certain index minerals (Atherton & Brotherton, 1972),

or with respect to the major iron oxide phase (Chinner, 1960; Hounslow & Moore, 1967; McLellan, 1985). However, samples with similar porphyroblasts commonly have different Fe–oxide combinations, and vice versa. A fourth approach is to classify samples using their whole-rock geochemical compositions, but whole-rock analyses were not obtained for all samples due to varying degrees of retrogression.

Recognising that no one approach is clearly the best, we have opted to use a combination of the above approaches. Samples were classified into four types based on a combination of: the porphyroblastic silicate minerals present in the assemblage; the modal abundance of muscovite and biotite; the colour of biotite; the dominant texture of rocks in hand specimen (e.g. schistose vs granoblastic); and the layer(s) in which they are found. Table 1 summarises these defining features. Despite the attempt to group samples using the above approach, there can be overlap in individual characteristics amongst different groups.

Rocks were first divided into two classifications based on whether garnet was observed in the mineral assemblage (Fig. 2). Type G samples (n = 13) are garnet-bearing and contain porphyroblastic staurolite and red-brown biotite; they also contain kyanite, sillimanite, both, or neither (Fig. 2), and occur in layers one, three, and four (Fig. 1c). Type K samples (n = 9) are kyanite-bearing, garnet-free, and contain green biotite (one sample lacks kyanite); they occur in layers one, two, and four (Fig. 1c). Two further categories comprise rocks that have distinctive mineral assemblages or textures and are spatially restricted to a single layer. Type M samples (n = 7) are schistose, muscovite-rich (> 15%, but typically >30%), biotite-poor (< 3%, but typically 0%; Fig. 2), and occur in layer one (Fig. 1c). Type C samples (n = 3) are cordierite-bearing and occur in layer three as nodule-rich horizons along the shores of Whetstone Lake (Fig. 2).

MINERAL ASSEMBLAGES AND TEXTURES

The following section describes mineral assemblages and textures for each classification type given above. Samples in the same category may show differences in the size and shape of individual

Table 1: Sample classifications (types) used in this study and a comparison of their defining features

	Type G	Type K	Type M	Type C
Name	Garnet-bearing	Kyanite-bearing (all but one sample) Grt-free	Muscovite-rich	Cordierite-bearing
Occurrence	Layers 1, 3, 4	Layers 1, 2, 4	Layer 1	Layer 3
Dominant texture	Porphyroblastic	Granoblastic	Schistose	Noduled
Muscovite abundance	Moderate to poor	Moderate to poor	Rich	Moderate to poor
Biotite abundance	Moderate	Rich	Poor to none	Moderate to poor
Biotite colour	Red-brown	Green	Green	Green or red-brown
Fe–oxides	Ilmenite	Ilmenite, Magnetite, Titanohematite	Ilmenite, Magnetite, Titanohematite	Ilmenite, Titanohematite
Plagioclase	Oligoclase to Andesine	Oligoclase to Andesine	Albite to Oligoclase	Oligoclase to Andesine

minerals, as well as different inclusion relationships between minerals. Because this study focuses on the peak metamorphic mineral assemblages however, no attempt was made to correlate different textural features in samples to differences in the P–T path by which samples reached peak conditions.

Type G: Garnet-bearing

In outcrop, type G samples appear weathered brown in colour, with visible porphyroblastic garnet and staurolite (Fig. 3a, d, g); in thin section, they contain biotite, garnet, staurolite, quartz, plagioclase, and ilmenite, with combinations of muscovite, kyanite, and sillimanite (Fig. 2). Where present, muscovite ranges from ~0.1 mm, tabular grains that define the foliation, to randomly orientated, coarse flakes (Fig. 3b, c, e). Biotite typically forms part of the matrix, occasionally defining a strong foliation, but may also be porphyroblastic (Fig. 3b, c, e, f, h). Garnet varies in appearance from ~0.5 mm grains included within staurolite to ~2 mm grains of a similar size to staurolite, to ~5 mm grains containing inclusions of staurolite (Fig. 3b, c, f, h). Plagioclase is part of the fine-grained (~ 0.2 mm) matrix in samples from layers three and four, whilst in layer one, plagioclase occurs as ~1 mm porphyroblasts with inclusions of graphite, quartz, biotite, and muscovite in their cores (Fig. 3b). Ilmenite is the only Fe–oxide observed in type G rocks; grains are elongate, typically contain many small (~ 10 μm) inclusions of quartz and may be aligned in the micaceous foliation (Fig. 3i). Ilmenite varies from unaltered to completely replaced by leucoxene, both within and between individual samples (Fig. 3i).

Type K: Kyanite-bearing (garnet-free)

In outcrop, garnet-free type K samples are dark in colour and most commonly granoblastic, with inconspicuous porphyroblasts (Fig. 4). Type K samples contain kyanite in a matrix of muscovite, biotite, quartz, and plagioclase (Fig. 2). One sample from Type K lacks kyanite but has been included in this group because it lacks garnet, has green biotite, contains sillimanite, and occurs in the sillimanite zone. Type K samples have different combinations and modal abundances of staurolite, sillimanite, and Fe–oxides (ilmenite, magnetite, and titanohematite; Fig. 2). Biotite is dark green in colour in type K samples, in contrast to its red-brown colour in type G samples (Fig. 3 and Fig. 4). Muscovite, biotite, and plagioclase exhibit the same range of textures as type G rocks (Fig. 4). Staurolite is typically euhedral and poikiloblastic, and ranges from ~1 mm to >5 mm in diameter (Fig. 4b, c). Kyanite ranges from blocky and inclusion-poor to fibrous in radiating splays (Fig. 4a, b, d). In samples K8 and K9, knots of fibrolite lie within or close to biotite (Fig. 4a). Most type K samples

are ilmenite-bearing, with some additionally containing small (~ 0.2 mm) grains of magnetite (Fig. 2). In two samples (K2 and K3), titanohematite is the major Fe–oxide phase, forming abundant, anhedral grains in the matrix (Fig. 4d). Titanohematite grains contain ~1- to 5-μm-thick ilmenite lamellae, which appear disjointed and discontinuous across grains (Fig. 4d).

Type M: Muscovite-rich

In outcrop, type M samples are silvery and schistose, as well as porphyroblastic (Fig. 5). Type M samples are muscovite-rich and have different combinations and modal abundances of aluminous minerals (staurolite, kyanite, and sillimanite; Fig. 2) and Fe–oxides (ilmenite, magnetite, and titanohematite; Fig. 2). Muscovite occurs as ~0.2 mm tabular grains that define the foliation (Fig. 5). Biotite is present in low modal abundance in five of seven type M samples, occurring as ~0.5 mm grains (Figs. 2, 5). Plagioclase in type M samples has a distinctive habit, occurring as large (5–10 mm), rounded porphyroblasts that are rich in inclusions of quartz and ilmenite or titanohematite, and show replacement to sericite at their rims (Fig. 5). Staurolite ranges from small inclusions (~ 0.1 mm) in garnet to large (~ 5 mm) porphyroblasts (Fig. 5a, b). Kyanite occurs as individual porphyroblasts, or intergrown with staurolite (Fig. 5c). Sillimanite occurs as knots of fibrolite either in the matrix or enveloping staurolite. Where present, magnetite is porphyroblastic and 0.5 to 2 mm in diameter (Fig. 5b, c). The matrix Fe–oxide phase is either ilmenite or titanohematite, both of which exhibit leucoxene alteration (Fig. 5).

Type C: Cordierite-bearing

In outcrop, type C samples are light grey with bulbous cm-sized cordierite porphyroblasts that weather proud of the outcrop surfaces (Fig. 6). There are two major varieties of Type C rocks: muscovite+kyanite-bearing and muscovite-free, staurolite+cordierite-bearing (Ms–Bt–Ky–Crd–Qz–Pl–Hem vs Bt–Grt–St–Crd–Qz–Pl–Ilm–Po ± Oam; Fig. 6). Biotite, plagioclase, quartz, and ilmenite form a fine-grained, occasionally foliated (< 1 mm) matrix in all samples (Fig. 6). Biotite is green in muscovite+kyanite-bearing rocks and brown in staurolite+cordierite-bearing samples (Fig. 6). In staurolite+cordierite-bearing samples, staurolite, garnet, and orthoamphibole form large (2 mm) porphyroblasts, whilst cordierite forms massive (>10 mm) poikiloblasts (Fig. 6b). The Fe–oxide phase ranges from titanohematite with minor patches of alteration to leucoxene in muscovite+kyanite-bearing samples to ilmenite with varying degrees of alteration to leucoxene in staurolite+cordierite-bearing samples (Fig. 6).
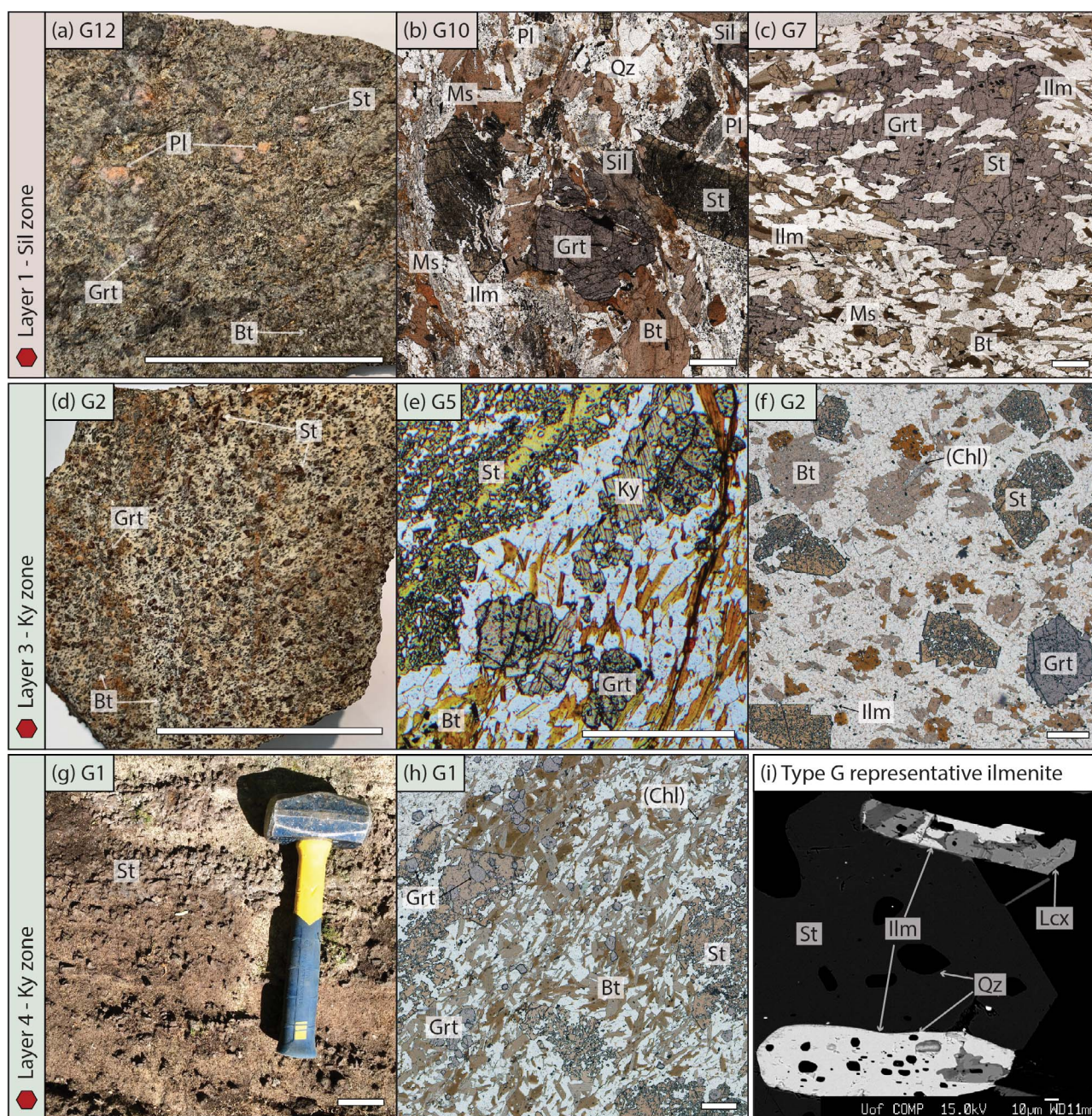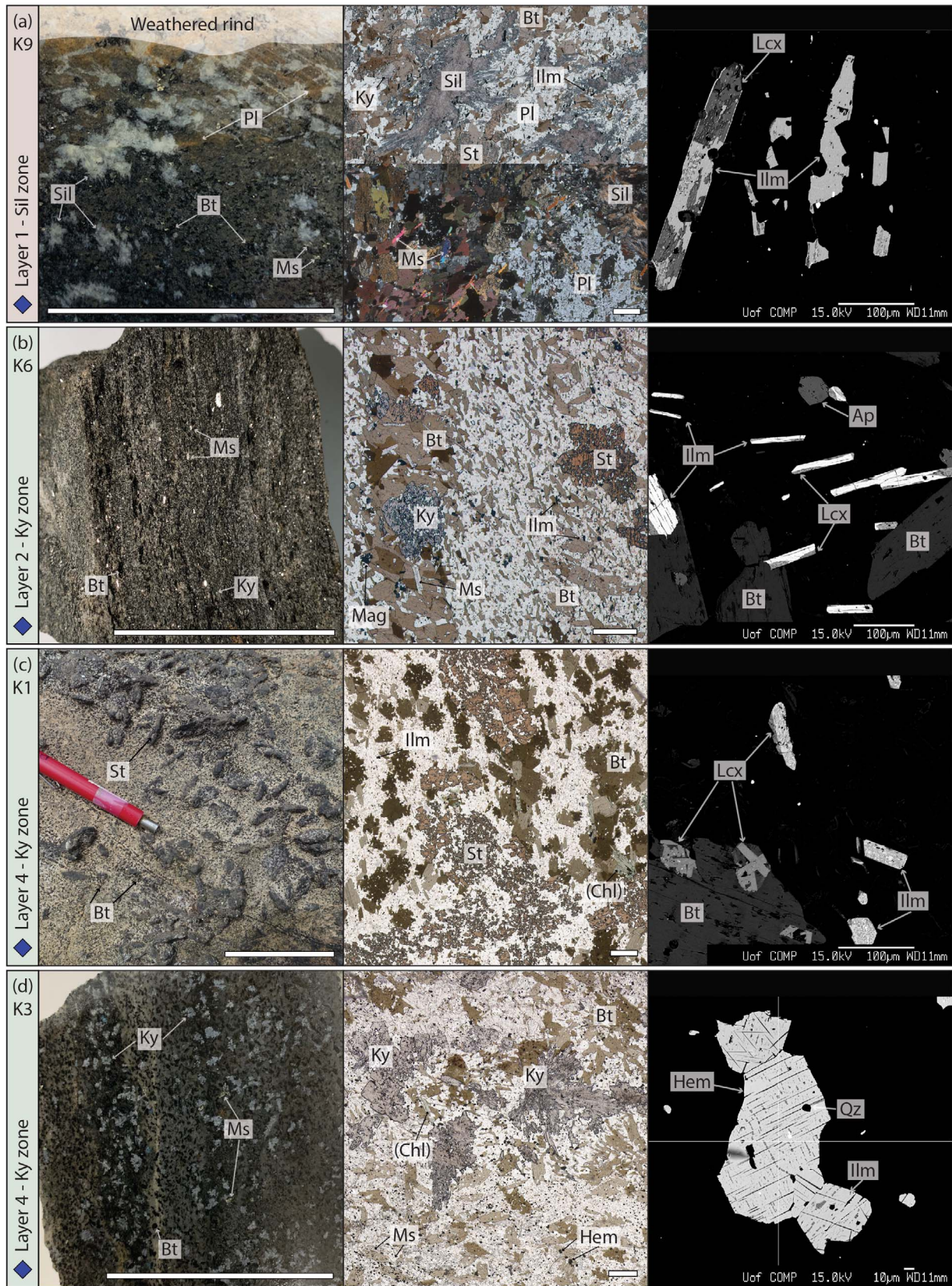
Fig. 3. Representative petrological features in type G samples shown in outcrop/hand-specimen photographs (scale bars = 5 cm), plane polarized light (PPL) thin section slide scans (scale bars = 1 mm), and BSE images. (a) Schistose porphyroblastic garnet–staurolite–biotite pelite. (b) Porphyroblastic staurolite, garnet, biotite, and plagioclase in a matrix of sillimanite, muscovite, quartz, and plagioclase. (c) Porphyroblastic garnet with inclusions of staurolite in a matrix of muscovite, quartz, and plagioclase. (d) Porphyroblastic garnet–staurolite–biotite pelite. (e) Foliated biotite schist with porphyroblasts of kyanite, staurolite, and garnet. (f) Porphyroblastic staurolite, garnet, and biotite in a matrix of quartz and plagioclase. (g) Porphyroblastic garnet–staurolite–biotite pelite. (h) Porphyroblastic staurolite with inclusions of garnet in a matrix of biotite, quartz, and plagioclase. (i) Representative image of ilmenite variably replaced by leucoxene in type G samples.

BULK COMPOSITIONAL VARIATIONS

Given the limited range in metamorphic grade, we examined whole-rock geochemical analyses to determine if differences in major element concentrations could explain the diversity of mineral assemblages. Sixteen of the 23 samples classify as true metapelites according to the criteria of Forshaw & Pattison (2023), the others classify as metagreywackes or low-K metasediments. Because the rocks are porphyroblastic, we nevertheless retain the general term 'metapelite' to describe all samples under consideration from Whetstone Lake.

Several key compositional parameters for metapelites are plotted in Fig. 7; on these diagrams our whole-rock geochemical analyses are contrasted with the median worldwide metapelite of Forshaw & Pattison (2023), as well as their database of pelitic analyses. Of the latter (5729 samples), only regions encompassing 50% of the compositional variability in pelites from that database are shown in Fig. 7a–c. In Fig. 7d involving loss-on-ignition (LOI), the shaded region encompasses 50% of the compositional variability of analyses from the porphyroblast and sillimanite zones of the database of

Fig. 4. Representative petrological features in type K samples shown in hand specimen photographs (scale bars = 5 cm), PPL and XPL (crossed polarised light) thin section slide scans (scale bars = 1 mm), and BSE images. (a) Sample K9. Porphyroblastic plagioclase, staurolite, and kyanite, with knots of fibrolite in a matrix of muscovite, quartz, and ilmenite. (b) Sample K6. Layered sample with porphyroblastic kyanite and staurolite, bimodally distributed biotite crystals, and a matrix of muscovite, quartz, plagioclase, ilmenite, and magnetite. (c) Sample K1. Porphyroblastic staurolite and biotite in a matrix of muscovite, quartz, plagioclase, and ilmenite. (d) Sample K3. Porphyroblastic kyanite and biotite in a matrix of muscovite, quartz, plagioclase, and titanohematite with ilmenite lamellae.
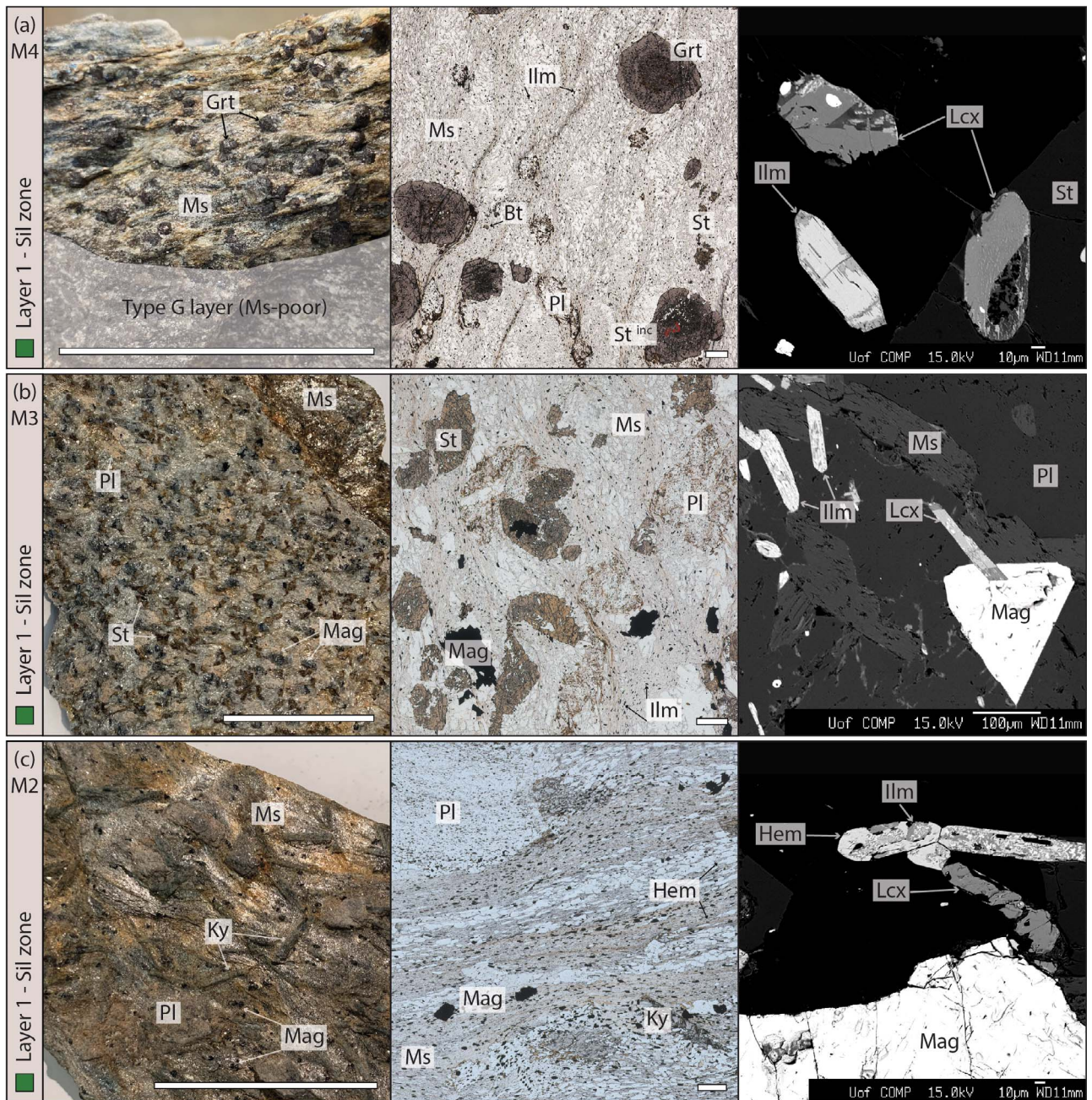
Fig. 5. Representative petrological features in type M samples shown in hand specimen photographs (scale bars = 5 cm), PPL thin section slide scans (scale bars = 1 mm), and BSE images. (a) Sample M4. Porphyroblastic garnet and plagioclase in a matrix of quartz, ilmenite, and foliated muscovite. (b) Sample M3. Porphyroblastic staurolite, plagioclase, and magnetite in a matrix of quartz, ilmenite, and foliated muscovite. (c) Sample M2. Porphyroblastic kyanite, plagioclase, and magnetite in a matrix of quartz, titanohematite, and foliated muscovite.

Forshaw & Pattison (2023) because LOI is strongly dependent on metamorphic grade.

Fig. 7a shows the AFM diagram of Thompson (1957). Analyses were manipulated and projected in the same manner as the worldwide database for consistency in our comparison. All Fe was converted to FeO. An amount of molar Fe equivalent to the molar Ti was removed, as part of projection from ilmenite. To take account of the compositional effects of variable proportions of quartz, plagioclase, and lithic fragments in the original sediment, compositions were projected from apatite, albite, and anorthite, in addition to muscovite, quartz, and H_2O.

The Whetstone Lake samples show a wide range of $A^{Ms} = $ molar $(Al_2O_3 - 3 \times K_2O)/(Al_2O_3 - 3 \times K_2O + FeO^{total} + MgO)$ from

-0.10 to 0.58, and $X_{Mg}^{proj} = $ molar $MgO/(FeO^{total} + MgO)$ from 0.08 to 0.58 (Fig. 7a). Twelve samples lie within the cluster of worldwide metapelite analyses, whilst ten lie outside this cluster, most of which have higher A^{Ms} than the average pelite (Fig. 7a). Type G and K samples span a range of X_{Mg}^{proj} from ~ 0.2 to 0.5 (Fig. 7a). Type M samples are more Fe-rich than the other types and have relatively high A^{Ms} (Fig. 7a). The single muscovite-bearing type C sample is more magnesian than all other samples, with $X_{Mg}^{proj} = 0.58$ and a relatively low A^{Ms} (Fig. 7a). Concerning compositional differences between the four layers, all samples from layer one have relatively high A^{Ms}, plotting above the idealised compositions of garnet and chlorite (Fig. 7a). Samples from layers two, three, and four have relatively lower A^{Ms}, plotting either
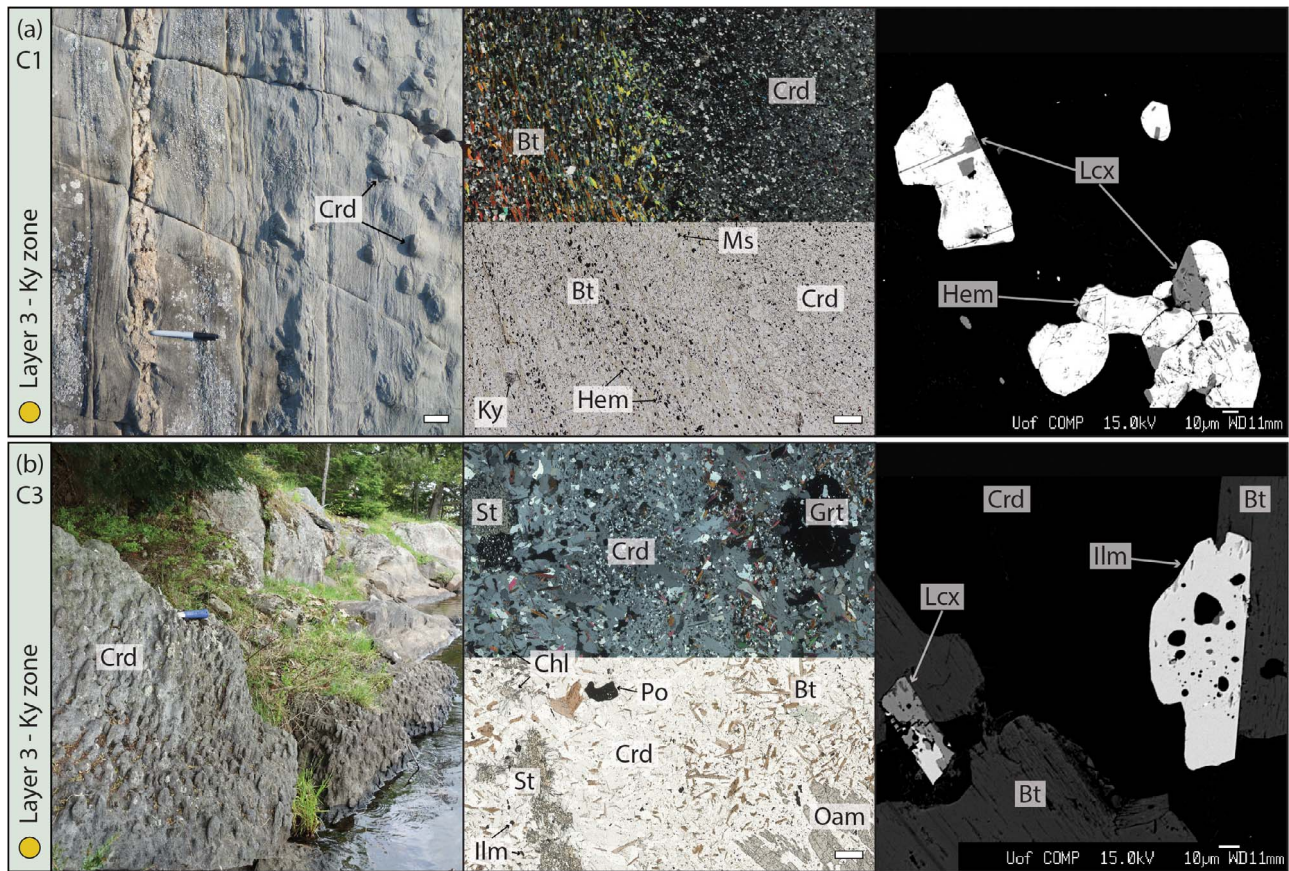
Fig. 6. Representative petrological features in type C samples shown in outcrop photographs (scale bars = 5 cm), PPL and XPL thin section slide scans (scale bars = 1 mm), and BSE images. (a) Sample C1. Poikiloblastic cordierite with small kyanite crystals in a foliated biotite, muscovite, quartz, and titanohematite matrix. (b) Sample C3. Porphyroblastic staurolite, garnet, and orthoamphibole within massive poikiloblastic cordierite. Biotite, quartz, plagioclase, and ilmenite make up the matrix and inclusions.

at or below the idealised compositions of garnet and chlorite (Fig. 7a).

Fig. 7b shows samples from Whetstone Lake plotted on the AKF diagram of Spear (1993), modified after Eskola (1915). Only three samples lie within the cluster of worldwide metapelite analyses, whilst twenty lie outside (Fig. 7b). Type G and K rocks cluster together between the idealised compositions of staurolite, cordierite, and biotite (Fig. 7b). Type M rocks are the most aluminous and potassic of any type, lying closest to the idealised component of muscovite (Fig. 7b), a mineral which is modally abundant in these rocks (Fig. 2). Sample C3 has the lowest potassium content of any rock, plotting far from the idealised component of muscovite (Fig. 7b), consistent with muscovite being absent from its assemblage (Fig. 2).

Fig. 7c plots $X_{Fe^{3+}} = 2 \times Fe_2O_3/(2 \times Fe_2O_3 + FeO)$ in moles versus $X_{Mg}^* = MgO/(FeO + MgO)$ in moles (noting that FeO in this case is measured FeO rather than all Fe converted to FeO). Only eight samples lie within the cluster of worldwide metapelite analyses, whilst 15 lie outside, most of which have higher $X_{Fe^{3+}}$ (Fig. 7c). X_{Mg}^* broadly increases from type M to G to K to C samples, as was seen in Fig. 7a. Samples containing titanohematite (e.g. C1, M1, M2, K2, and K3) typically have the highest $X_{Fe^{3+}}$, with the result that X_{Mg}^* is markedly higher than X_{Mg}^{proj} (Fig. 7a, c).

Fig. 7d shows the variation in MnO and loss on ignition (LOI) for Whetstone Lake samples. Twenty samples lie within the cluster of worldwide metapelite analyses, whilst three lie outside, two due to their low MnO contents (Fig. 7d). Garnet-bearing type G samples and garnet-free type K samples commonly have similar MnO contents (Fig. 7d). Type M samples are low in MnO (< 0.02 wt.%), except for sample M4 which contains garnet and has MnO = 0.04 wt.% (Fig. 7d). Garnet-bearing and garnet-free type C samples have similar MnO contents (Fig. 7d).

MINERAL COMPOSITIONAL VARIATIONS

Having established that the diversity of mineral assemblages in the kyanite and sillimanite zones at Whetstone Lake reflects a range of bulk compositions, we explored how mineral compositions vary with respect to the four classifications. The following analysis focuses on key mineral compositional parameters that will later be used to test the predictions of thermodynamic modelling. All analysed minerals except for garnet exhibit largely homogeneous compositions, with no substantial variation within individual samples.

Biotite has Si = 5.37–5.64 cations, Ti = 0.09–0.25 cations, Al = 3.10–3.58 cations, Na = 0.03–0.12 cations, and K = 1.62–1.80 cations. Muscovite has Si = 6.04–6.29 cations, Ti = 0.03–0.06 cations, Al = 5.28–5.74 cations, Na = 0.23–0.43 cations, and K = 1.50–1.83 cations. Whole-rock X_{Mg}^* and biotite X_{Mg}^* increase concomitantly in samples that contain five modal per cent or more biotite (Types G, K, and C; Fig. 8a). In type M rocks, which have less than five modal per cent biotite, biotite X_{Mg}^* is significantly higher than whole-rock X_{Mg}^* (Fig. 8a). There is no correlation between the number of Ti cations in biotite and whole-rock TiO_2 (Fig. 8c); however, the number of Ti cations in biotite is lower in titanohematite-bearing samples than in ilmenite-bearing
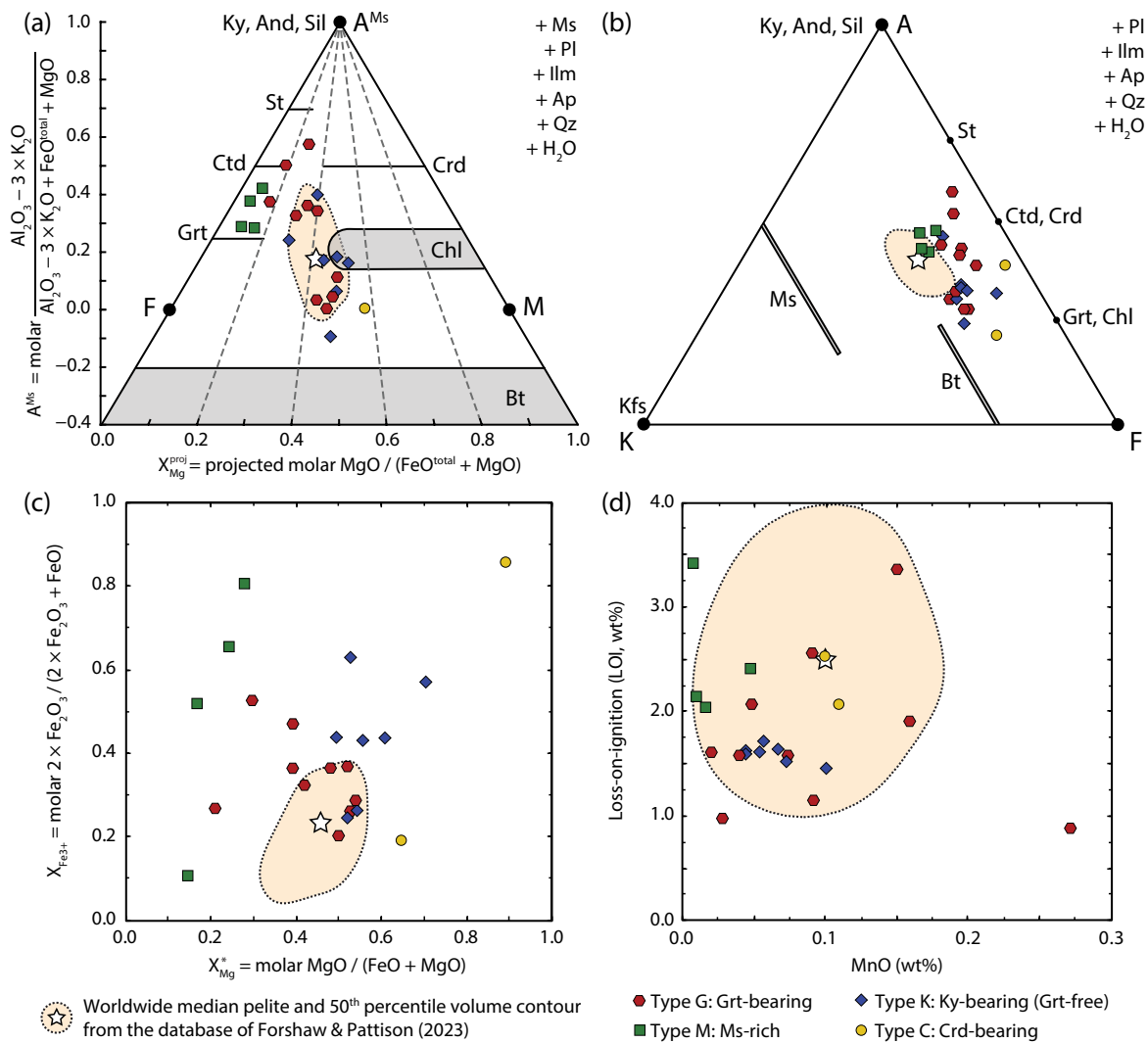
Fig. 7. Distribution of the 23 whole-rock analyses of this study versus the median worldwide pelite (white star; Forshaw & Pattison, 2023) and a region encompassing 50% of the analyses from the database of Forshaw & Pattison (2023). (a) AFM diagram after Thompson (1957), mineral stabilities after Spear (1993). (b) AKF diagram after Eskola (1915), modified according to Spear (1993). (c) X_{Mg}^* versus $X_{Fe^{3+}}$. (d) MnO versus LOI.

samples, and biotite has higher X_{Mg}^* in the former (Fig. 8c). The same correlation has been documented in west-central Maine, where for a given grade of metamorphism, the Ti content of biotite decreases as its Mg/Fe ratio increases (Guidotti *et al.*, 1977; Henry & Guidotti, 2002; Henry *et al.*, 2005). There is no significant correlation between whole-rock A^{Ms} and the number of Al cations in biotite or muscovite (Fig. 8b, e); however, the number of Al cations in biotite and muscovite is comparatively lower in titanohematite-bearing samples (e.g. C1, M1, M2, K2, K3; Fig. 8b, e). Muscovite in titanohematite-bearing samples also contains a higher total number of Fe cations (Fig. 8f; c.f. Labotka, 1980).

In garnet, X_{Mg}^* increases concomitantly with whole-rock X_{Mg}^* from type M to G to C rocks (Fig. 9b). The number of Mn and Ca cations in garnet show no correlation with whole-rock MnO and CaO contents (Fig. 9a, c). EPMA compositional maps of garnet reveal a range of zoning patterns in Fe, Mg, Ca, and Mn. These are described in detail below because of their importance to the calculation of bulk compositions for phase equilibrium modelling. Concerning manganese, in half the samples, it exhibits smooth core to rim concentric decreases ($\Delta X_{Sps} > 0.02$ between core and rim; Fig. 9a, d, f, g; c.f. Atherton & Edmunds, 1966;

Harte & Henley, 1966; Hollister, 1966), whilst in the other half, it shows relatively flat compositional zoning ($X_{Sps} < 0.01$; Fig. 9a, e). Sharp increases in manganese content occur at the rims of subhedral garnets with embayed margins, a feature commonly ascribed to resorption and concomitant fractionation (accumulation) in its preferred host (garnet) as it is consumed (Fig. 9f; de Béthune *et al.*, 1975; Kohn & Spear, 2000). Concerning X_{Mg}^*, in five samples, it increases from core to near-rim ($\Delta X_{Mg}^* > 0.03$), whilst in 11 samples, it is relatively constant across the garnet ($\Delta X_{Mg}^* < 0.02$). Concerning calcium, in two samples, it increases from core to near-rim ($\Delta X_{Grs} = 0.01$–0.02; Fig. 9c, f), in nine samples, it decreases from core to near-rim ($\Delta X_{Grs} = 0.02$–0.14; Fig. 9c, e), and in five samples, it is relatively constant across the garnet ($\Delta X_{Grs} < 0.01$; Fig. 9c, d, g). Within these gradients, X_{Grs} exhibits a patchy distribution at the micron scale (Fig. 9d, e, f, g). In layer one, dark, fluid inclusion-rich, patchy regions in garnet show lower X_{Grs} contents (Fig. 9f). Previous authors have interpreted similar features to be the result of dissolution–reprecipitation reactions occurring along the rims and cracks within garnet (Hames & Menard, 1993; Whitney *et al.*, 1996; Martin *et al.*, 2011; Dempster *et al.*, 2019, 2017; Wolfe *et al.*, 2021).
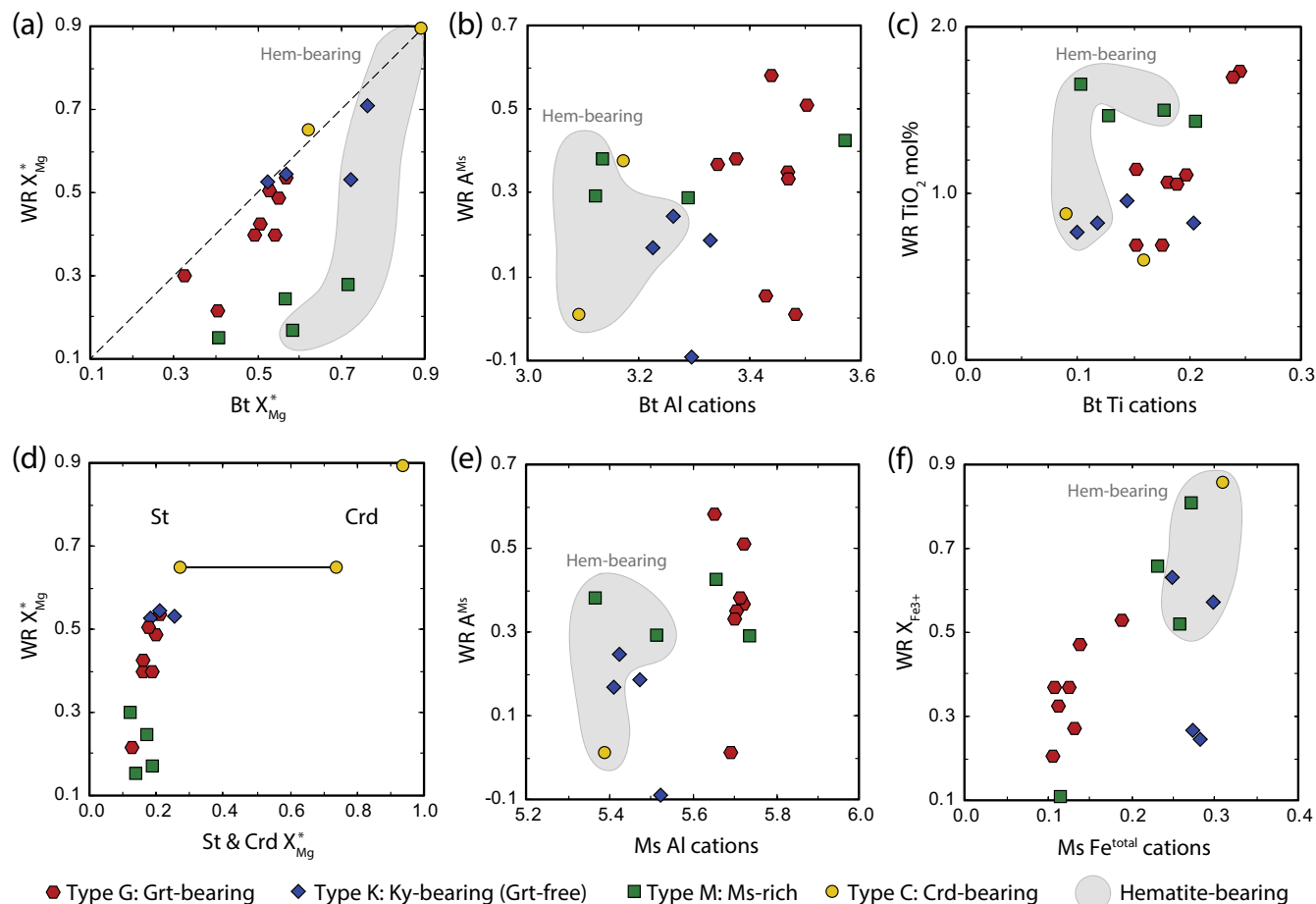
Fig. 8. Compositional diagrams depicting the variation of mineral compositions with whole-rock composition. (a) Biotite X^*_{Mg} versus whole-rock X^*_{Mg}. (b) Biotite Al cations versus whole-rock A^{Ms}. (c) Biotite Ti cations versus whole-rock TiO_2. (d) Staurolite and cordierite X^*_{Mg} versus whole-rock X^*_{Mg}. (e) Muscovite Al cations versus whole-rock A^{Ms}. (f) Muscovite Fe^{total} cations versus whole-rock $X_{Fe^{3+}}$. Titanohematite-bearing samples are highlighted by the grey region.

Whole-rock X^*_{Mg} and staurolite X^*_{Mg} show a positive correlation (Fig. 8d). Staurolite is most magnesian in sample C3 where it coexists with cordierite (Fig. 8d). Based on two samples, there is an increase in cordierite X^*_{Mg} with whole-rock X^*_{Mg} (Fig. 8d). In type G/K/C samples, the anorthite content of plagioclase ranges mostly between 0.20 and 0.40, whilst in type M samples plagioclase is albitic (Table S7). A close correlation exists between whole-rock and plagioclase Na/Ca ratios, as has been noted in other studies (Pattison & Debuhr, 2015; Pattison & Goldsmith, 2022).

## INFLUENCES ON MINERAL ASSEMBLAGE DEVELOPMENT AT WHETSTONE LAKE

The diversity of assemblages within the kyanite and lower sillimanite zones at Whetstone Lake indicate that bulk composition exerts the primary influence on mineral assemblage development. The importance of X_{Mg} has long been documented in metapelites (Barth, 1936; Thompson, 1957), with authors commonly describing contrasts in mineral assemblages during progressive metamorphism as a function of bulk rock X_{Mg} (Thompson, 1976a, 1976b; Atherton, 1977). Several studies have documented variation in mineral assemblages from individual metamorphic zones, which are the result of differences in whole-rock X_{Mg} (Atherton & Brotherton, 1972; Guidotti, 1974; Guidotti et al., 1975; Labotka, 1981, 1980; Lang, 1991; Ford, 2002; Harte, 2022).

When plotted on an AFM diagram, only 6.7% of the samples in database of Forshaw & Pattison (2023) have X^{proj}_{Mg} less than 0.20 or greater than 0.55 (Fig. 2A of that paper); whereas at Whetstone Lake, eight of the 32 samples examined here (25%) lie outside of this compositional range.

Fig. 10 shows an AFM diagram plotting the stable assemblages for samples from Whetstone Lake based on average measured mineral compositions (c.f. Cesare, 1999; Guidotti et al., 1975; Lang, 1991; Lang & Rice, 1985; Pattison, 1987; Pigage, 1982). Assemblages for seven representative samples are shown using X_{Mg} instead of X^*_{Mg}. There is a general progression of stability fields increasing in X_{Mg} from garnet-bearing type G samples to garnet-free type K samples to cordierite-bearing type C samples. Stable assemblages for muscovite-rich type M samples occur across a range of X_{Mg} (Fig. 10). Whole-rock analyses for each sample lie close to the stability fields for their assemblage (Fig. 10).

Garnet-bearing type G samples are distinguished from garnet-free type K samples by their lower X^*_{Mg} (Fig. 7c). Cordierite-bearing type C samples have higher X^*_{Mg} than any other type (Fig. 7c). In addition to X^*_{Mg}, cordierite stability is also dependent on K_2O content, with cordierite commonly occurring in muscovite-free metagreywackes (e.g. Crd–St–Oam–Grt-bearing sample C3; Eskola, 1915; Kamineni, 1979; Kamineni et al., 1991; Lal & Shukla, 1975; Moore & Waters, 1990; Vallance, 1967). The high X^*_{Mg} in cordierite–
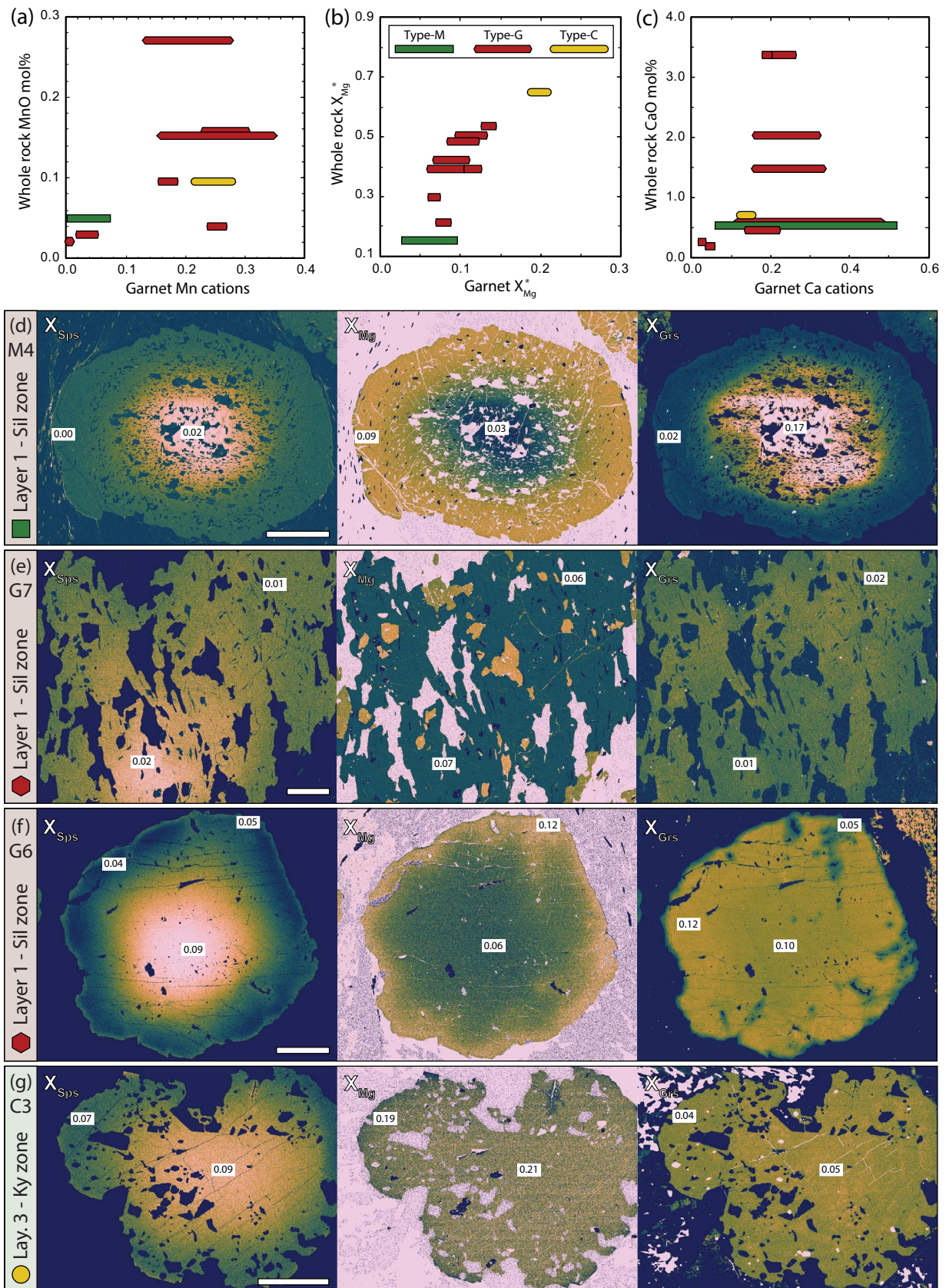
Fig. 9. (a) Garnet Mn cations versus whole-rock MnO. (b) Garnet X^*_{Mg} versus whole-rock X^*_{Mg}. (c) Garnet Ca cations versus whole-rock CaO. All compositional ratios and cation amounts for garnet are depicted as a range between maximum and minimum values from line profiles. (d/e/f/g) Compositional maps (X_{Sps}, X_{Mg}, and X_{Grs}) of garnet zoning from four representative samples. Scale bar is 1 mm. Images are coloured using the scientific colour map 'batlow' (Crameri, 2021) after thresholding maximised compositional differences within garnet.

kyanite–muscovite-bearing sample C1 is probably a consequence of high $X_{Fe^{3+}}$, highlighting the interplay between these two variables (Fig. 7c).

$X_{Fe^{3+}}$ is the primary control on the type and modal abundance of Fe–oxide present in the sample (Chinner, 1960; Hounslow & Moore, 1967; Diener & Powell, 2010; Forshaw & Pattison, 2021). Concerning the ferromagnesian silicates, staurolite is an Fe-rich mineral that is observed in all ilmenite- and magnetite-bearing samples but is absent or a minor component of titanohematite-bearing samples. The instability of staurolite in titanohematite-bearing samples is probably due to high X_{Mg}^* related to high $X_{Fe^{3+}}$. However, some samples have high $X_{Fe^{3+}}$, as well as low X_{Mg}^*, owing to low MgO contents; the absence of staurolite and occurrence of kyanite and sillimanite in these rocks appears to be due to high $X_{Fe^{3+}}$ (Ganguly, 1972).

Whilst X_{Mg}^* and $X_{Fe^{3+}}$ can explain many of the differences in mineral assemblage observed at Whetstone Lake, other compositional parameters also exert an influence. In Type M rocks, the abundance of muscovite is a result of high K_2O and Al_2O_3 content (Fig. 7b). MnO content appears critical to garnet stability in type M rocks; samples are typically garnet-free and low in MnO (< 0.02 wt.%), except for sample M4 which contains garnet and has MnO = 0.04 wt.% (Fig. 7d). Comparatively, garnet-bearing type G samples and garnet-free type K rocks have similar MnO contents, indicating that the presence of garnet in type G samples is more strongly influenced by low X_{Mg}^* than by MnO content (Fig. 7c, d). Al_2O_3 content and by extension A^{Ms} appear to have little effect on the observed mineral assemblages, modal proportions, and mineral compositions.

PHASE EQUILIBRIUM MODELLING CONSIDERATIONS

The wide range of mineral assemblages in metapelites from the kyanite and lower sillimanite zones of Whetstone Lake, make these rocks an ideal suite to test the ability of thermodynamic modelling to reproduce mineral assemblages, modal abundances, and mineral compositions in diverse bulk compositions.

Sample choice

For our analysis, we only considered samples for which the whole-rock geochemical composition, mineral compositions, and modal abundances had all been determined (Table S1). Because our phase equilibrium modelling necessitates that the model system has been closed and that it achieved thermodynamic equilibrium at peak P–T conditions, unaffected by later events, we excluded samples which contain obvious non-equilibrium phenomena. These include those with multiple aluminosilicates (e.g. G9, G12, G13, K2, and K9) and those in which garnet is partially broken down to sillimanite and/or contains extensive dark, fluid inclusion-rich patches (e.g. G9–G13).

To capture the range of mineral assemblages and whole-rock geochemical compositions, two samples from each of the four different rock types were selected for phase equilibrium modelling. The two rocks from Type G are G2, which contains the Al_2SiO_5-free assemblage Grt–St–Ms–Bt–Pl–Qz–Ilm, and G6, which contains the sillimanite-bearing assemblage Grt–St–Sil–Ms–Bt–Pl–Qz–Ilm. The two rocks from Type K are K4, which contains the staurolite+ilmenite-bearing assemblage Ky–St–Ms–Bt–Pl–Qz–Ilm, and K3, which contains the staurolite-absent, titanohematite-bearing assemblage Ky–Ms–Bt–Pl–Qz–Hem. The two rocks from Type M are M4, which contains the aluminosilicate-free, garnet+staurolite+ilmenite-bearing
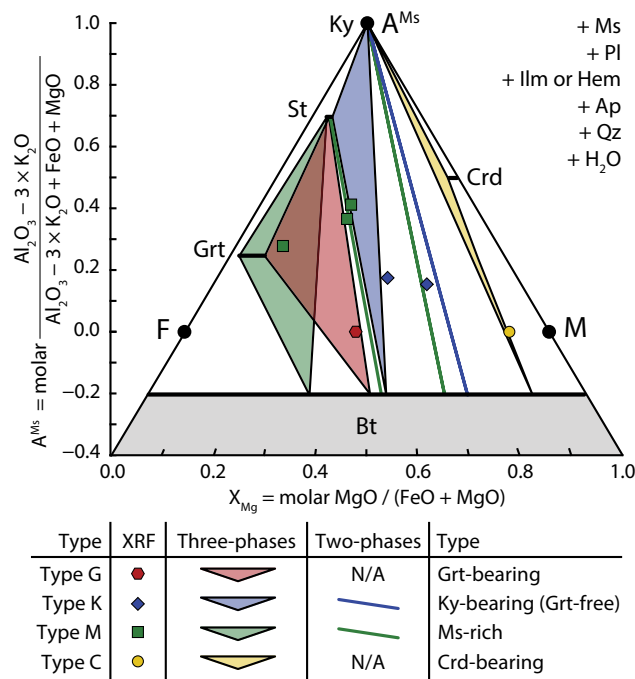
Fig. 10. AFM diagram showing the plotting positions of minerals from seven representative samples (G2, K3, K4, M2, M4, M5, and C1) using EPMA-measured mineral compositions. Three-phase assemblages are denoted by fields and two-phase assemblages by lines. Corresponding whole-rock analyses (XRF + titration) are shown as coloured symbols.

assemblage Grt–St–Ms–Bt–Pl–Qz–Ilm, and M2, which contains the staurolite-absent, kyanite+titanohematite-bearing assemblage Ky–Ms–Bt–Pl–Qz–Mag–Hem. The two rocks from Type C are C1, which contains the kyanite+titanohematite-bearing assemblage Ky–Crd–Ms–Bt–Pl–Qz–Hem, and C3, which contains the cordierite+orthoamphibole+ilmenite-bearing assemblage Grt–St–Crd–Ged–Pl–Qz–Ilm.

Bulk composition

Whole-rock versus local bulk composition

As described above, bulk composition exerts a primary control on predicted phase assemblages, proportions, and compositions in phase equilibrium modelling. However, determining an effective bulk composition for phase equilibrium modelling is a nontrivial task, and carries significant implications for the applicability of the results (Lanari & Engi, 2017).

Many authors use a whole-rock XRF analysis as an estimate of an effective bulk composition. A problem with this approach is that the rock volume analysed by XRF may not be the same as that from which the thin section is cut (see Fig. 1 of Duesterhoeft & Lanari, 2020). Some studies have shown that whilst an XRF-derived phase diagram may reproduce the mineral assemblage observed, the predicted mineral proportions do not correlate well with those observed in the thin section (Guevara & Caddick, 2016; Palin et al., 2016). A consequence is that P–T results derived from mineral compositional isopleths may be flawed (Lanari & Engi, 2017).

Alternatively, a local bulk composition can be determined by combining modal abundance estimates of phases with representative compositions (e.g. Carson et al., 1999; Forshaw et al., 2019; George et al., 2022; Gopon et al., 2022), or making an X-ray map of a representative area of a thin section (e.g. de Hoÿm de Marien et al., 2019; Lanari et al., 2019, 2014; Marmo et al., 2002).

Phase diagrams constructed using local bulk compositions, in which differing modal abundances may be estimated, may more satisfactorily reproduce mineral proportions and compositions (Zeh, 2001; Palin et al., 2016; Lanari & Duesterhoeft, 2019; Zou et al., 2022). A difficulty with this approach is that judgment must be exercised in estimating the appropriate volumes and compositions of minerals assumed to have interacted at peak conditions.

In our study, we adopted both methods and compared the results. We refer to local bulk compositions as 'MADE' and whole-rock bulk compositions as 'XRF' in the text, figures, and tables. Local bulk compositions were determined by combining modal abundance estimates of phases with representative compositions presented in Tables S4 and S6–18. Garnet was incorporated in local bulk compositions by combining representative core and rim analyses with estimates of the volume proportion of garnet core and rim. For Fe–oxide phases with volumetrically significant lamellae (Fig. 4d), a recombined ilmenite/titanohematite analysis was calculated based on the ratio of lamellae to host determined from representative backscattered electron images. All other minerals exhibit largely homogeneous compositions, with no substantial variation within individual samples.

Fractionation

Several workers have detailed the unreactive nature of porphyroblasts during the prograde metamorphism of pelites (Chinner, 1965; Ridley, 1985; Ridley & Thompson, 1986; Waters & Lovegrove, 2002; Pattison & Tinkham, 2009; Pattison et al., 2011; Carlson et al., 2015; Pattison & Spear, 2018). Compositional zoning in garnets from Whetstone Lake indicates that they did not completely re-equilibrate with the matrix during growth. Fractionation of garnet in phase equilibrium modelling is considered to have a significant effect on mineral assemblage stability fields and compositional isopleths when its mode exceeds two volume percent (Evans, 2004; Tinkham & Ghent, 2005; Zuluaga et al., 2005; Gaidies et al., 2008a, 2008b, 2006; Moynihan & Pattison, 2013; Lanari & Engi, 2017). In samples G2 and C3, garnet occurs in minor modal abundance ($0.2 \pm 0.8\%$ and $0.8 \pm 1.5\%$, respectively; Fig. 2) and is relatively homogeneous in composition (Fig. 8g); therefore, garnet was not subtracted from the bulk composition in the phase equilibrium modelling of these two samples. In samples G6 and M4, garnet is abundant ($6.6 \pm 2.2\%$ and $12.0 \pm 2.7\%$, respectively; Fig. 2) and exhibits pronounced compositional zoning (Fig. 8d, f); therefore, the interior portions of garnet were subtracted from the bulk composition in the phase equilibrium modelling of these two samples. We included 10% of the original volume of garnet. The garnet composition was assumed to be that of the near-rim in sample G6 where the garnet exhibits an increase in Mn at its rim, and that of the rim in sample M4 where no such increase is observed. This procedure was only possible for the local bulk composition (MADE) because for whole-rock bulk compositions (XRF), modal abundances were not available. We refer to these new fractionated local bulk compositions as 'FRAC' in the text, figures, and tables.

Note that whilst the largest garnet in each thin section was typically chosen for analysis, we cannot ensure that this garnet was centrally sectioned or was the largest garnet contained in the rock. Therefore, garnet core compositions subtracted as part of our fractionation calculation probably do not represent the core composition of the first nucleated garnet. However, this makes no difference to our calculations because peak P–T conditions were examined and not the path along which garnet grew. Garnet may have also been subject to later diffusional modification during cooling from peak P–T conditions which would affect the compositions used in our calculations. Assuming cooling from peak temperature conditions of ~675°C (upper amphibolite facies) at 1°C/Myr (the slowest cooling rate suggested for the Grenville; Cosca et al., 1992), Fe, Mn, and Mg would diffuse <250 μm within garnet (Caddick et al., 2010). Given that the analysed garnets are 3–4 mm in diameter, compositional profiles will not have been substantially modified from those present at peak P–T conditions.

Bulk composition comparison

Table 2 compares whole-rock (XRF) and local (MADE and FRAC) bulk compositions for each sample. Consistent differences between these include relatively higher SiO_2 in whole-rock bulk compositions, and relatively higher FeO and K_2O in all but one of the local bulk compositions. For ilmenite-bearing samples G2, G6, and K4, $X_{Fe^{3+}}$ is higher by >0.10 in whole-rock bulk compositions than in local bulk compositions (Table 2); whereas for ilmenite-bearing samples M4 and C3, whole-rock $X_{Fe^{3+}}$ and local $X_{Fe^{3+}}$ values are similar (< 0.05 difference). In titanohematite-bearing samples, K3, M2, and C1, whole-rock $X_{Fe^{3+}}$ and local $X_{Fe^{3+}}$ values are also similar (< 0.07 difference). Fractionated compositions for samples G6 and M4 are also included in Table 2; these show considerably lower FeO and MnO contents when compared to local bulk compositions without fractionation, owing to the removal of garnet.

Fig. 11 plots whole-rock and local bulk compositions on AFM and AKF diagrams. A^{Ms} for local bulk compositions ranges from relatively higher than whole-rock bulk compositions to lower than whole-rock bulk compositions (Fig. 10a). X_{Mg}^{proj} is higher in all but one of the local bulk compositions when compared to whole-rock bulk compositions (Fig. 10a). In the AKF diagram, there are no consistent trends to higher or lower AKF values when comparing whole-rock and local bulk compositions (Fig. 10b).

Oxidation state

A rock's oxidation state and its influence on the stability of mineral assemblages is commonly expressed in terms of oxygen fugacity (fO_2), oxygen activity (aO_2), or the chemical potential of oxygen (μO_2). These are thermodynamic conventions that allow variations in redox state to be expressed assuming oxygen gas is the electron receptor/donor, even though the exchange of electrons in the system of interest may not involve free oxygen gas. A more direct, if less rigorous, measure of oxidation state is the ratio of Fe_2O_3 to total iron (e.g. $X_{Fe^{3+}}$, also termed oxidation ratio), assuming that iron is overwhelmingly the most abundant element with more than one valence state in the rock (Chinner, 1960; Evans, 2006; Diener & Powell, 2010). However, $X_{Fe^{3+}}$ is not a simple function of fO_2 or aO_2 (Frost, 1991), being dependent on the $X_{Fe^{3+}}$ contents of co-existing silicates and oxide minerals, and on their modal abundances. In most natural rocks, classic fO_2-buffering mineral assemblages like quartz–fayalite–magnetite or hematite–magnetite do not occur. If they do occur, they are not expected to persist over a range of grade (and thus to actively 'buffer' the fO_2 of the rock) because of competition with other minerals in the rock for the Fe^{3+}.

When considering the interaction of rocks with fluids of different aO_2, an open-system process in which fluid infiltrates the rock and either introduces or removes O_2 or redox-sensitive elements like S or C, aO_2 is the natural variable to consider when describing the oxidation state of the reacting system (Diener & Powell, 2010). In reactive systems in which the only fluid involved is that which is lost through thermally triggered devolatilization reactions and

Table 2: Bulk rock compositions (mol. % oxide) used to calculate phase diagrams

Sample	Type	SiO_2	TiO_2	Al_2O_3	Fe_2O_3	FeO	MnO	MgO	CaO	Na_2O	K_2O	X^*_{Mg}	$X_{Fe^{3+}}$	$X^{model}_{Fe^{3+}}$	Q_{asm}	Q_{vol}	Q_{cmp}
Median Worldwide Pelite (Forshaw & Pattison, 2023)		71.53	0.76	12.91	0.75	4.90	0.08	4.01	0.78	1.49	2.81	0.46	0.23	N/A	N/A	N/A	N/A
G2	XRF	69.08	0.68	11.38	0.70	5.47	0.04	5.43	2.98	2.22	2.04	0.50	0.20	0.05	100	71	36
	MADE	54.71	0.57	20.43	0.52	10.14	0.07	7.54	2.00	1.68	2.35	0.43	0.09	0.05	100	94	39
G6	XRF	67.16	1.05	14.18	1.76	6.13	0.27	3.95	1.94	2.29	1.27	0.39	0.37	0.05	100	84	44
	MADE	64.40	1.07	13.39	0.41	9.89	0.25	6.09	1.22	1.36	1.93	0.38	0.08	0.05			
	FRAC	66.30	1.16	13.35	0.40	7.82	0.05	6.28	1.06	1.47	2.10	0.45	0.09	0.05	88	91	34
K4	XRF	62.92	0.95	14.95	1.04	5.85	0.05	6.86	2.48	2.63	2.25	0.54	0.26	0.10	100	85	45
	MADE	58.01	0.47	18.91	0.44	8.08	0.08	7.74	1.89	2.00	2.36	0.49	0.10	0.10	86	91	47
K3	XRF	69.49	0.76	12.39	1.90	2.87	0.07	6.86	1.70	1.83	2.13	0.71	0.57	0.60	100	78	52
	MADE	56.96	1.87	16.71	3.70	4.54	0.16	8.88	2.22	2.30	2.65	0.66	0.62	0.60	100	93	49
M4	XRF	66.91	1.43	15.00	0.57	9.67	0.05	1.67	0.41	1.38	2.93	0.15	0.10	0.05	100	87	61
	MADE	65.26	2.25	16.75	0.33	8.78	0.07	1.03	0.60	1.34	3.58	0.11	0.07	0.05			
	FRAC	69.42	2.66	17.29	0.24	3.69	0.01	0.65	0.20	1.59	4.24	0.15	0.12	0.05	100	91	60
M2	XRF	68.96	1.65	16.46	4.07	1.98	0.01	0.76	0.25	3.45	2.40	0.28	0.80	0.75	100	91	43
	MADE	64.64	1.84	16.82	5.46	3.98	0.01	0.55	0.43	3.50	2.76	0.12	0.73	0.75	100	97	44
C1	XRF	70.52	0.87	10.08	2.82	0.96	0.11	7.80	2.61	2.65	1.58	0.89	0.85	0.86	75	71	33
	MADE	67.24	0.53	11.47	4.34	1.42	0.23	10.99	1.22	1.42	1.14	0.89	0.86	0.86	78	79	50
C3	XRF	72.18	0.60	11.15	0.58	4.95	0.09	9.01	0.34	0.56	0.53	0.65	0.19	0.05	100	88	25
	MADE	70.42	1.65	8.91	0.71	7.26	0.22	9.64	0.11	0.45	0.64	0.57	0.16	0.05	100	96	26
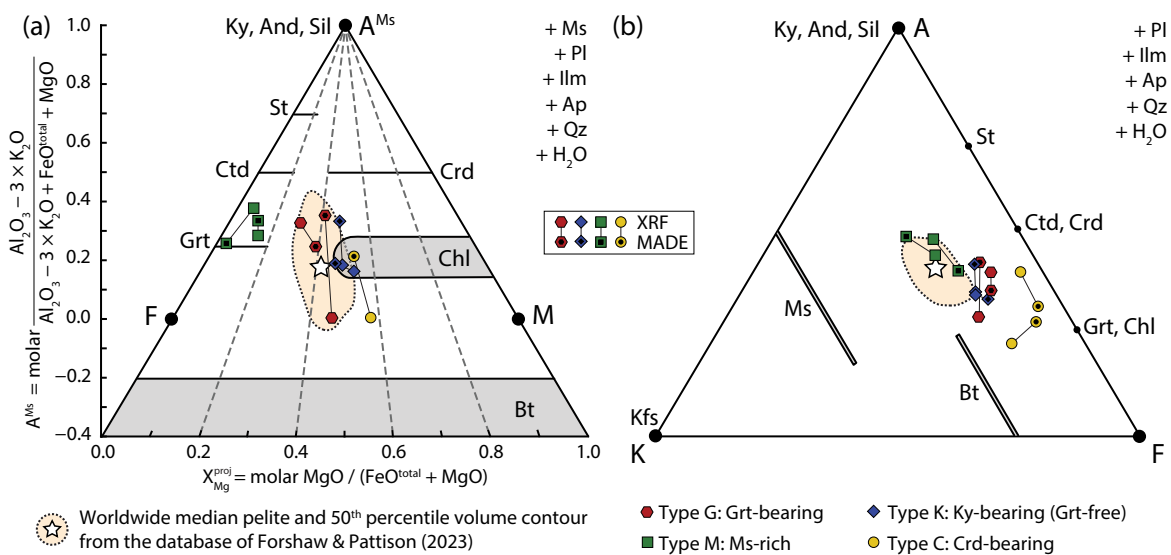
Fig. 11. AFM and AKF diagrams showing the difference between whole-rock (XRF) and local (MADE) bulk compositions for each sample.

in which iron is the dominant valence-dependent element, $X_{Fe^{3+}}$ (or the amount of oxygen) may be the most appropriate redox-sensitive variable to use (Diener & Powell, 2010). This is because the capacity for electron exchange exerted by the rock, through its mineral assemblage, is much greater that that exerted by the metamorphic fluids released (Eugster, 1972; Thompson Jr, 1972; Rumble, 1978; Dyar *et al.*, 2002). Consequently, for the phase equilibrium modelling below, the oxygen content of each rock was fixed based on the ratio of ferrous to ferric iron in the sample.

Determination of the proportion of total iron in the bulk composition that was Fe^{3+} (i.e. whole-rock $X_{Fe^{3+}}$) follows the recommendations of Forshaw and Pattison (p 19, 2021). Whole-rock $X_{Fe^{3+}}$ measured by titration was considered a maximum due to surface weathering processes or post-crushing, pre-analysis oxidation (Hillebrand, 1908; Fitton & Gill, 1970; Reay, 1981;

Diener & Powell, 2010; lo Pò & Braga, 2014). A second bulk $X_{Fe^{3+}}$ value was calculated for the local bulk composition by combining estimates of Fe^{3+} in minerals with modal abundances. The uncertainty on this value was estimated by constructing *maximum* and *minimum* $X_{Fe^{3+}}$ local bulk compositions, obtained by combining the modal abundances with mineral compositions in which $X_{Fe^{3+}}$ had either been maximised or minimised. For biotite, muscovite, chlorite, and staurolite, the standard deviations from Forshaw & Pattison (2021) were used to determine maximum and minimum $X_{Fe^{3+}}$ in these minerals. For orthoamphibole, the constraints from Hawthorne *et al.* (2012) were used to determine maximum and minimum $X_{Fe^{3+}}$ values. For garnet, ilmenite, titanohematite, and magnetite, $X_{Fe^{3+}}$ values were kept constant at a value determined by the charge-balancing method of Droop (1987).

The $X_{Fe^{3+}}$ values obtained from the two methods were then plotted on T–$X_{Fe^{3+}}$ phase diagrams and compared with the

predicted mineral assemblages. The value of $X_{Fe^{3+}}$ chosen for subsequent P–T phase diagram modelling was that for which the predicted Fe–oxide from thermodynamic modelling matched the observed Fe–oxide, at a value which fell as close as possible to the whole-rock $X_{Fe^{3+}}$ values determined above (Table 2). This approach ensured that the whole-rock $X_{Fe^{3+}}$ used for modelling is consistent with the thermodynamic data set and solution models chosen, as is discussed below (Forshaw & Pattison, 2021).

Fluid composition

Interlinked with the oxidation state of a metamorphic rock is the composition of the fluid produced during metamorphism. Metamorphic fluids comprise some combination of H_2O, nonpolar gases (chiefly CO_2), salts, and rock-derived solutes (Ferry & Burt, 1982; Yardley & Bodnar, 2014; Manning, 2018; Evans & Tomkins, 2020). Whilst thermodynamic properties for salts and aqueous complexes are available (Helgeson & Kirkham, 1976; Shock et al., 1992, 1989; Pokrovskii & Helgeson, 1997; Sverjensky et al., 1997; Miron et al., 2017), as well as solution models describing their mixing (Helgeson & Kirkham, 1974; Helgeson et al., 1981; Dolejš, 2013; Dubacq et al., 2013), these are typically calibrated at pressures less than 5 kbar. Recent work has expanded their applicability to higher pressures, but there are few experimental data with which to compare and test calculations (Galvez et al., 2015; Connolly & Galvez, 2018). Therefore, the most complex fluid that phase equilibrium modelling studies consider presently is a C–O–H–S mixture (Evans et al., 2010). Oxygen was not considered a fluid component in our calculations (see previous section). The only sulphur-bearing phase identified in Whetstone Lake samples was pyrrhotite (present in 4 of the 32 samples, of which only sample C3 was modelled). Given the minor modal amount of pyrrhotite and uncertainty on whether it represents a prograde or retrograde phase, sulphur was also excluded as a component. Graphite was present in 8 of the 32 samples, of which two were chosen for modelling. A C–O–H fluid produced from devolatilization reactions in the presence of excess graphite has uniquely determined thermodynamic properties at a specified P–T condition (Connolly & Cesare, 1993). Plotting the P–T conditions of typical Barrovian staurolite–kyanite-bearing samples in fig. 1 of Connolly & Cesare (1993) shows that $a_{H_2O} > 0.95$. Therefore, our modelling considers a pure H_2O fluid that was assumed to be in excess.

Thermodynamic database

Of the thermodynamic databases currently available, only the data set of Holland & Powell (2011) and associated solution models of White et al. (2014a) incorporate all the Fe^{3+}-bearing phases relevant for the rocks studied here (see Forshaw & Pattison, 2021 and Pattison & Goldsmith, 2022, for discussions of different thermodynamic data sets). The following solution models were used: chlorite, biotite, garnet, chloritoid, staurolite, cordierite, orthopyroxene, muscovite, paragonite, and silicate melt (White et al., 2014a, 2014b); plagioclase and K-feldspar (Holland & Powell, 2003); epidote (Holland & Powell, 2011); orthoamphibole (Schorn & Diener, 2019); ilmenite–hematite (White et al., 2000, 2014a, 2014b); magnetite–spinel (White et al., 2002). The orthoamphibole solution model was only activated when modelling sample C3. The margarite solution model was omitted in all calculations due to the prediction of a margarite stability field in metapelitic rocks that is not observed in nature (White et al., 2014a), although the margarite endmember in the muscovite and paragonite solution models was still incorporated. Pure phases included quartz, albite, rutile, titanite, and the aluminosilicates.

Calculation of phase diagrams

Phase diagrams were computed in the 11-component MnNCKF-MASHTO system ($MnO–Na_2O–CaO–K_2O–FeO–MgO–Al_2O_3–SiO_2–H_2O–TiO_2–O_2$), using Theriak-Domino version 2022.12.18 (de Capitani & Brown, 1987; de Capitani & Petrakakis, 2010). Firstly, isobaric $T–X_{Fe^{3+}}$ (bulk rock) equilibrium assemblage diagrams at a pressure of 5 kbar were constructed for the eight samples using both whole-rock (XRF) and local (MADE or FRAC) bulk compositions. This initial 5 kbar pressure estimate was chosen owing to occurrence of sillimanite+staurolite-bearing, kyanite+staurolite-bearing, and sillimanite+kyanite+staurolite-bearing mineral assemblages in close proximity, suggestive of pressures between 4 and 7 kbar (Carmichael, 1978; Carmichael et al., 1978; White et al., 2014a; Pattison & Spear, 2018). Estimates of $X_{Fe^{3+}}$ were made using the approach described above. P–T equilibrium assemblage diagrams were then calculated for the eight samples using both whole-rock (XRF) and local (MADE or FRAC) bulk compositions at the specified value of $X_{Fe^{3+}}$. After identification of a stable assemblage field (see below), $T–X_{Fe^{3+}}$ diagrams were recalculated at a pressure matching that found on P–T equilibrium assemblage diagrams to ensure the estimates of $X_{Fe^{3+}}$ fitted the approach described above.

METHOD OF ANALYSIS OF MODELS VERSUS NATURE

Identification of a stable assemblage field

A stable assemblage field that matched the observed assemblage was identified on the pairs of phase diagrams (calculated for the XRF, and MADE or FRAC, compositions) for the eight rocks. In diagrams where no predicted field exactly matched the interpreted assemblage, the one with the closest match to the observed assemblage was chosen. In this approach, higher priority was given to the more modally abundant silicates, with less weight given to modally minor phases. A reference P–T point within each field was then selected for comparison with the observed mineral abundances and compositions. Where there was latitude in the placement of samples in the predicted stability fields, we placed samples from the sillimanite zone at higher temperatures than those from the kyanite zone. In addition, where possible, we chose the reference P–T point to be the same in the phase diagrams calculated using whole-rock and local bulk compositions. As will be discussed below, it was not always possible to adhere to these two criteria given the restricted stability fields of certain assemblages in the phase diagrams. An important point is that variations in the placements of our P–T points are of relatively minor consequence to our analysis of the models because the predicted mineral compositions show small variations within individual assemblage fields.

Quality factors

A method was sought to quantitatively compare the predicted mineral assemblages, proportions, and compositions in the phase diagrams with the natural observations. Some previous studies have qualitatively compared the topology of phase diagrams between data sets against natural observations (Kendrick & Indares, 2018; Santos et al., 2019). Others have focussed on modal abundances and compositions, making quantitative comparisons between observations and predictions (Forshaw et al., 2019; García-Arias, 2020; Starr et al., 2020; Gervais & Trapy, 2021). In these studies, it is difficult to gauge the overall performance of the models in predicting the natural observations

since authors typically focus on one or a few specific aspects for comparison (e.g. mineral assemblage, mineral modes, or mineral compositions). In our study, it proved challenging to rationalise the fit amongst phase assemblages, abundances, and compositions for sixteen different phase diagrams.

An alternative approach involves the calculation of *quality factors* for the fit between thermodynamic prediction and nature (Duesterhoeft & Lanari, 2020). This approach was introduced in the program Bingo-Antidote that was designed for iterative thermodynamic modelling calculations (Lanari *et al.*, 2017; Lanari & Duesterhoeft, 2019; Duesterhoeft & Lanari, 2020; Lanari & Hermann, 2021). This software compares the predicted phase assemblage, proportions, and compositions with natural observations and determines a quantitative measure of the degree of mismatch. The procedure involves the calculation of three model quality factors which quantify the degree to which the model reproduces the observed phase assemblages (Q_{asm}), abundances (Q_{vol}), and compositions (Q_{cmp}). The quality factors used here are based on those described by Duesterhoeft & Lanari (2020) and the reader is referred to that paper for a detailed description of their calculation. The quality factors used in our study are similar, but not identical, to those in Duesterhoeft & Lanari (2020), as described below.

Q_{asm} evaluates the degree to which the predicted and observed assemblages match; it is calculated by dividing the number of matching phases by the total number of phases in the observed and predicted assemblages, and multiplying by 100 (Duesterhoeft & Lanari, 2020). Q_{vol} evaluates the degree to which the predicted and observed modal abundances match. For each phase (i), Q_i^{vol} is calculated from the average of the predicted and observed mode multiplied by the normalised degree of fit between the predicted and observed mineral mode; a total Q_{vol} is then calculated using the square root of the sum of these individual mineral mode quality factors (Q_i^{vol}), multiplied by 100 (Duesterhoeft & Lanari, 2020). Q_{cmp} evaluates the degree to which the predicted and observed compositions match and is calculated using several steps. First, the relative analytical uncertainty of element concentrations in the natural minerals ($\pm\sigma_{i,j}$) is compared with the difference ($\Delta_{i,j}$) between the observed ($X_{i,j}^{obs}$) cations per formula unit for elements (j) and phases (i) listed in Table 3, and the predicted values ($X_{i,j}^{pred}$). Bingo-Antidote calculates the relative analytical uncertainty ($\pm\sigma_{i,j}$) using the variation in composition for a set of pixels in an EPMA X-ray compositional map (Duesterhoeft & Lanari, 2020). The standard deviation of a homogeneous population of WDS spot analyses is typically half the relative analytical uncertainty ($\pm\sigma_{i,j}$) calculated from X-ray compositional maps (Lanari, pers. comm., 2021). In our study, we, therefore, used two standard deviations ($\pm 2\sigma_{i,j}$) on our homogeneous population of WDS spot analyses in place of the relative analytical uncertainty ($\pm\sigma_{i,j}$) used by Duesterhoeft & Lanari (2020). Our comparison of $\Delta_{i,j}$ with $2\sigma_{i,j}$ first considers the 2σ and 12σ boundary conditions: if $\Delta_{i,j} < 2\sigma_{i,j}$ for our analyses, then $Q_{i,j}^{cmp} = 100\%$. If $(\Delta_{i,j} - \sigma_{i,j}) > 12\sigma_{i,j}$ for our analyses, then $Q_{i,j}^{cmp} = 0\%$. If $\Delta_{i,j}$ lies between these boundary conditions then $Q_{i,j}^{cmp} = \left(1 - \left(\left(\Delta_{i,j} - 2\,\sigma_{i,j}\right)/12\sigma_{i,j}\right)\right)^{X_{i,j}^{pred}+1}$ (Duesterhoeft & Lanari, 2020). Quality factors for each element ($Q_{i,j}^{cmp}$) were then averaged for each mineral and these values weighted based on the modal abundances of the observed phases, rather than the modal abundance of the predicted phases as was done in Duesterhoeft & Lanari (2020). Quality factors for each element ($Q_{i,j}^{cmp}$) were then averaged for each mineral and these values weighted based on the modal abundances of the observed phases, rather than

the modal abundance of the predicted phases as was done in Duesterhoeft & Lanari (2020). The weighted quality factors for each mineral were then summed to determine a total Q_{cmp} (Duesterhoeft & Lanari, 2020). Therefore, Q_{cmp} represents a combination of two variables: a mineral's modal abundance and a mineral's composition.

The above quality factors were used as a first-order assessment of the success of the phase equilibrium modelling. This was followed by a more detailed exploration of the compositions of specific minerals to determine if there were any consistent discrepancies in certain elements. Predicted and observed mineral compositions were portrayed in 1:1 plots to visualise the degree of compositional agreement or disagreement (e.g. Forshaw *et al.*, 2019).

RESULTS OF ANALYSIS OF MODELS VERSUS NATURE

An example of the above phase diagram modelling is shown in Fig. 12a–d for sample G2; this shows $T–X_{Fe^{3+}}$ and $P–T$ equilibrium assemblage diagrams calculated for both the whole-rock and local bulk compositions. Diagrams for the other seven samples are included as supplementary Figs. S5–11. In sample G2, an $X_{Fe^{3+}}$ of 0.20 was measured using XRF/titration and an $X_{Fe^{3+}}$ of 0.09 ± 0.06 was estimated from combining modal abundances with representative mineral compositions (Table 2; Fig. 12a, b). On the $T–X_{Fe^{3+}}$ diagrams, magnetite is predicted to be stable at $X_{Fe^{3+}} > 0.08$ and rutile is predicted to be stable at $X_{Fe^{3+}} < 0.05$ across the range of temperature conditions at 7.5 kbar (Table 2; Fig. 12a, b). Therefore, $P–T$ diagrams for sample G2 were calculated using an $X_{Fe^{3+}}$ of 0.05 for both bulk compositions to ensure that magnetite and rutile were not predicted (Table 2; Fig. 12). This value is lower than that determined from titration, but within uncertainty of $X_{Fe^{3+}}$ estimated in the local bulk composition (Table 2). Major differences between the two $P–T$ diagrams result from the large difference in Al_2O_3 content (Table 2; Fig. 12c, d). A predicted mineral assemblage field containing the observed assemblage (Grt–St–Ms–Bt–Pl–Qz–Ilm) was found on diagrams for both compositions (Fig. 12c, d). Whilst the sizes of the assemblage fields vary between the two bulk compositions (Fig. 12c, d), a common $P–T$ point of 620°C and 7.5 kbar could be identified on both diagrams. This was used as starting point for comparison between mineral proportions and compositions (Fig. 12c, d). This same process was undertaken for the other seven samples. Fig. 12e, f shows the predicted mineral assemblage fields and reference $P–T$ conditions for all eight samples calculated using both the whole-rock and local bulk compositions. Fig. 13 depicts the quality factors calculated at the reference $P–T$ conditions for all samples and bulk compositions. The following sections consider how well the models reproduced the observed assemblages, abundances, and compositions.
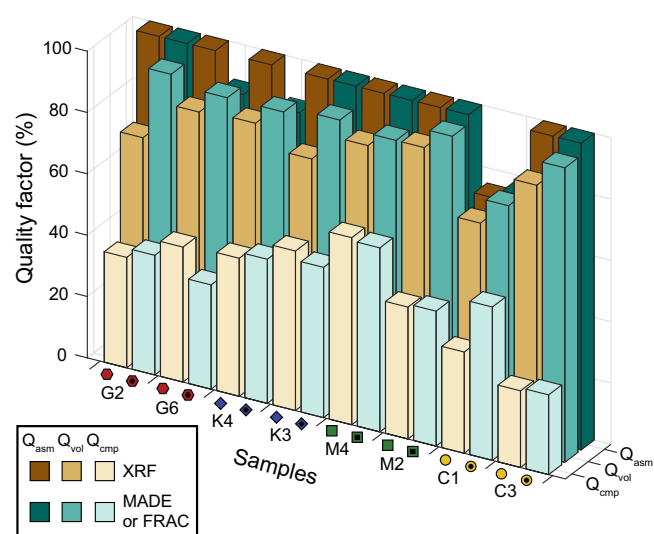
Assemblage

It was possible to locate a $P–T$ stability field containing an exact match to the observed assemblage for both the whole-rock and local bulk compositions in five of the eight samples (Fig. 13). In samples G6 and K4, an exact match was only found on diagrams constructed for whole-rock bulk compositions; on the diagrams constructed for the local bulk compositions, muscovite was missing from the predicted assemblage for sample G6 and ilmenite was missing from the predicted assemblage for sample K4, leading to lower Q_{asm} values (Fig. 13). In sample C1, neither the diagram constructed for the whole-rock or local bulk composition provided a match to the observed assemblage (Fig. 13); in the whole-rock bulk composition diagram, chlorite and muscovite are missing
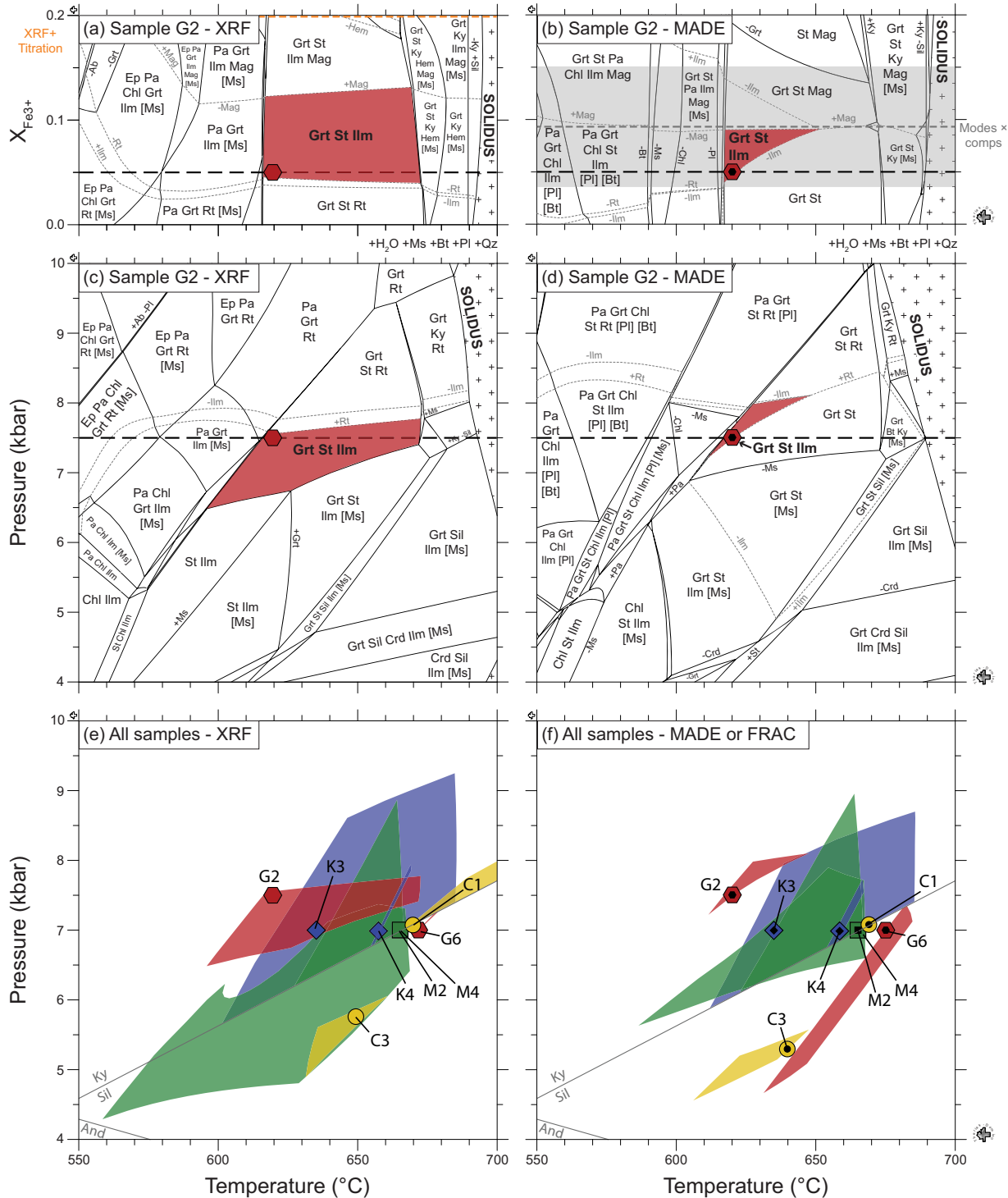
Fig. 12. (a) T–$X_{Fe^{3+}}$ equilibrium assemblage diagram calculated for the whole-rock bulk composition of sample G2. (b) T–$X_{Fe^{3+}}$ equilibrium assemblage diagram calculated for the local bulk composition of sample G2. (c) P–T equilibrium assemblage diagram calculated for the whole-rock bulk composition of sample G2. (d) P–T equilibrium assemblage diagram calculated for the local bulk composition of sample G2. Phases present across diagrams are listed in the header (e.g. +Ms). If absent, they are shown in square brackets (e.g. [Ms]). The orange short-dashed line in (a) represents the $X_{Fe^{3+}}$ value measured using XRF plus titration, whilst the grey short-dashed line and associated uncertainty band in (b) represents the $X_{Fe^{3+}}$ estimated from combining representative mineral compositions with modal abundances (see text for discussion). The black long-dashed lines in (a/b/c/d) show the pressure and $X_{Fe^{3+}}$ value used to calculate corresponding diagrams. Coloured fields show the matching peak assemblage. The red hexagon denotes the reference P–T conditions at which predicted phase abundances and compositions were compared with those observed. (e/f) P–T diagrams showing a compilation of the mineral assemblage fields and chosen P–T estimates (symbols) for the eight samples in this study. (e) Phase diagram calculated for whole-rock bulk compositions (XRF). (f) Phase diagram calculated for the local bulk composition (MADE or FRAC).

Table 3: Elements selected for comparison between observed and modelled mineral compositions in this study, and in turn used to calculate Q_{cmp}

	Si	Ti	Al	Fe^{3+}	Fe^{2+}	Mn	Mg	Ca	Na	K
Pl	X		X					X	X	X
Ms	X		X	X	X		X	X	X	X
Chl	X		X	X	X	X	X			
Bt	X	X	X	X	X	X	X			
Grt			X	X	X	X	X	X		
St		X	X	X	X	X	X			
Crd					X	X	X			
Oam	X		X	X	X		X	X	X	
Ilm/Hem		X		X	X	X	X			

Fig. 13. Bar chart comparing quality factors calculated for the eight samples using their whole rock bulk compositions (XRF) and either their local bulk composition (MADE or FRAC).

from the assemblage, whilst in the local bulk composition diagram, muscovite is missing and staurolite is predicted. The majority of our chosen assemblage fields overlap for both types of bulk composition at approximately 620–675°C and 6.5–7.5 kbar. In both diagrams, the predicted mineral assemblage for sample C3 occurs at lower pressure (4.5–6 kbar) than any other sample (Fig. 12). For sample G2, the predicted assemblage field for the local bulk composition occurs at relatively higher pressures and lower temperatures than for the whole-rock bulk composition (Fig. 12).

Modal abundances

Predicted modal abundances are typically close to those observed in all samples regardless of the bulk composition used for modelling ($Q_{vol} > 60\%$; Table 2; Fig. 13). However, Q_{vol} is always greater for local bulk compositions than whole-rock bulk compositions, with $Q_{vol} > 90\%$ for all local bulk compositions apart from sample C1 where the assemblage was poorly predicted (Table 2; Fig. 13). A similar result was found by Palin *et al.* (2016) who conducted modelling using the internally consistent thermodynamic data set 5.5 (Holland & Powell, 1998). Sample G2 is an example where the Q_{vol} is considerably higher for the local bulk composition (94%) than whole-rock bulk composition (71%; Table 2; Fig. 13). Because Q_{vol} is weighted based on the relative proportions of minerals, this discrepancy is primarily a result of poor predictions of modally

abundant phases. For sample G2, the phase diagram calculated for the whole-rock bulk composition overestimates plagioclase (predicted = 31% vs observed = 23 ± 3%) and significantly underestimates staurolite (predicted = 5% vs observed = 26 ± 3%).
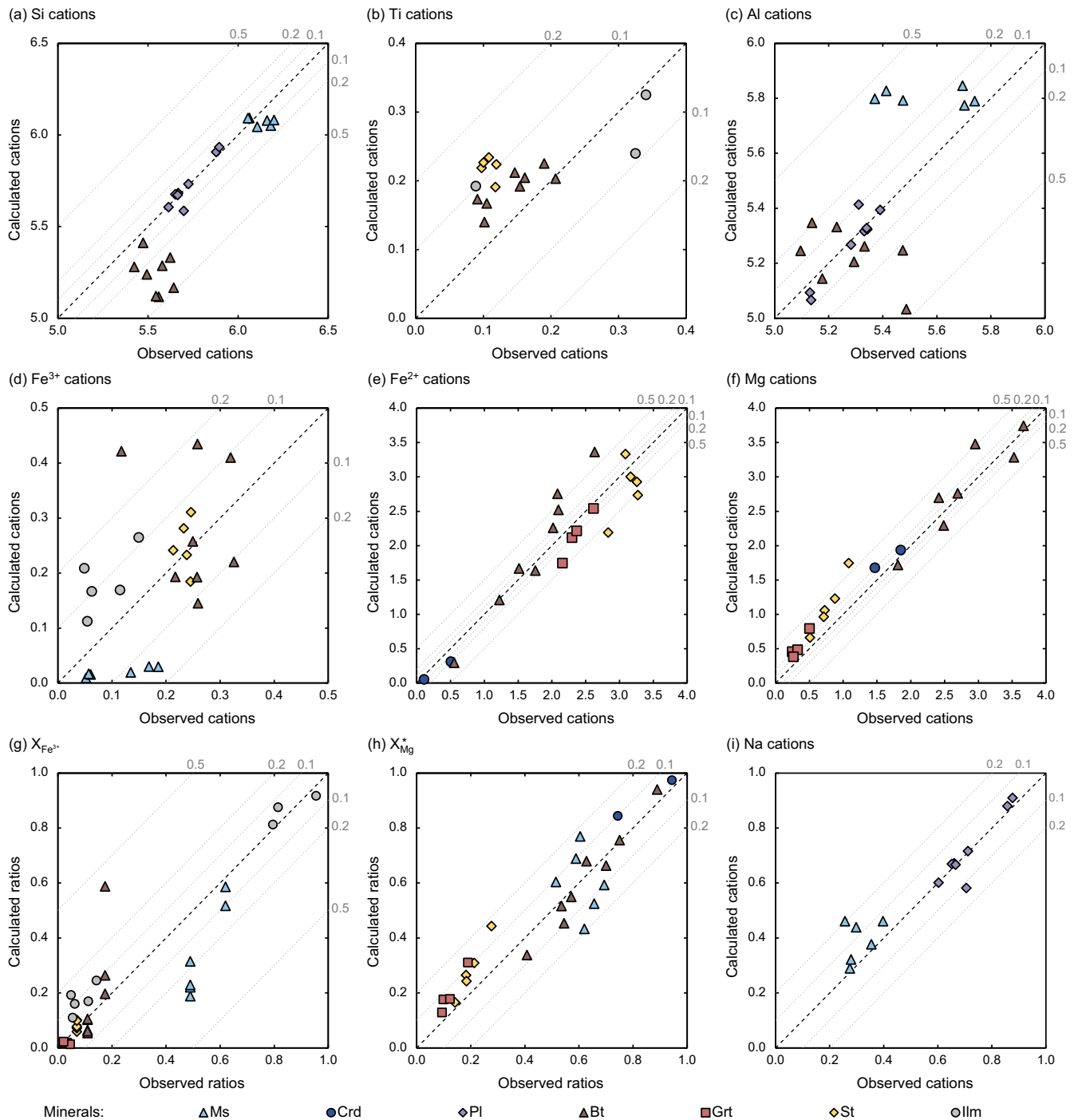
Mineral compositions

Mineral compositions are poorly predicted in most samples, with Q_{cmp} ranging from 25 to 61% (Fig. 13). Unlike Q_{vol}, Q_{cmp} is not significantly different for diagrams constructed using different bulk compositions (Fig. 13). To better understand the causes of the relatively poor Q_{cmp} factors, we compared predicted and observed compositions of all phases. Fig. 14 depicts several 1:1 plots in which predicted mineral compositions are compared to those observed. For ease of visualisation, only the compositions predicted for the local bulk composition are plotted on Fig. 14; however, this is of minor consequence to our comparisons because differences between the predicted mineral compositions for different types of bulk composition are small, as can be gauged from the similar Q_{cmp} values (Table 2; Fig. 13).

In biotite, the predicted number of Si cations is underestimated, whilst the predicted number of Ti cations is typically overestimated (Fig. 14a, b). The predicted number of Al, Fe^{3+}, and Mg cations show scatter about the 1:1 line with no obvious bias to lower or higher values (Fig. 14c, d, f). However, Fe^{3+} and $X_{Fe^{3+}}$ in biotite are overestimated when hematite is predicted to be part of the assemblage (Fig. 14d, g). Forshaw & Pattison (2021) found that whilst $X_{Fe^{3+}}$ in biotite increases from ilmenite- to magnetite- to hematite-bearing rocks, the increase in the number of Fe^{3+} cations in biotite in the same samples is minor. This indicates that the change in biotite $X_{Fe^{3+}}$ with oxidation state primarily results from the removal of Fe^{2+} cations and not an increase in the number of Fe^{3+} cations as is predicted in the current solution model. The number of Fe^{2+} cations in biotite is overestimated for four samples, underestimated for one sample, and similar to that observed in three samples (Fig. 14e). Biotite X_{Mg}^* is typically well reproduced by the model (Fig. 14h).

Concerning muscovite, the predicted number of Si, Na, and K cations typically match those observed (Fig. 14a, i). However, the predicted number of Al cations is overestimated, and the predicted number of Fe^{3+} cations is underestimated (Fig. 14c, d), as was found by Forshaw & Pattison (2021). The overestimation of the number of Al cations is typically correlated with an underestimation of the total Fe^{3+}, Fe^{2+}, and Mg content of muscovite.

Predicted compositions of garnet, staurolite, and cordierite underestimate Fe^{2+} and overestimate Mg (Fig. 14e, f); this results in a significant overestimation of X_{Mg}^* by 0.03 to 0.10 for cordierite, 0.04 to 0.12 for garnet, and 0.03 to 0.16 for staurolite (Fig. 14h). In staurolite, the predicted number of Fe^{3+} cations and $X_{Fe^{3+}}$

Fig. 14. Predicted versus observed mineral compositions. In order to depict all minerals together, some cation totals were shifted diagonally by subtracting or adding a specific number of cations to/from the calculated and observed values. (a) Si cations. For plagioclase, three cations have been added to the measured values. (b) Ti cations. (c) Al cations. For plagioclase, four cations have been added to the measured values, whereas for biotite, two cations have been added to the measured values. (d) Fe^{3+} cations. (e) Fe^{2+} cations. (f) Mg cations. (g) $X_{Fe^{3+}}$. (h) X_{Mg}^{*}. (i) Na cations. Those minerals for which the number of observed cations is well predicted by the models will lie on the 1:1 line. Grey dotted lines show cation differences between calculated and observed values.

broadly match the estimates in our samples, the latter taken from Forshaw & Pattison (2021; Fig. 14d), but the predicted number of Ti cations is consistently double that observed (Fig. 14b).

The predicted composition of plagioclase is close to that observed in every rock sample (Fig. 14a, c, i). This probably results from plagioclase's relatively simple composition and the relatively few phases that contain calcium and sodium end members (garnet = Ca; muscovite = Na). The predicted number of

Fe^{3+} cations in ilmenite, and in turn its $X_{Fe^{3+}}$, are overestimated by 0.05 to 0.20 (Fig. 14d, g). The orthoamphibole solution model (Schorn & Diener, 2019) was provided to the first author by Diener (written communication, 2021) who noted that it remains relatively untested. Despite this, the predicted number of Si, Mg, Ca, and Na cations typically match those observed. The predicted number of Al and Fe^{2+} cations is overestimated, whilst the predicted number of Fe^{3+} cations is significantly underestimated.

IMPLICATIONS FOR THERMODYNAMIC MODELLING

Phase equilibrium modelling using data set 6.2 (Holland & Powell, 2011) largely reproduces the diversity of mineral assemblages in the kyanite and lower sillimanite zones at Whetstone Lake. In addition, the P–T conditions of the different predicted assemblage fields broadly overlap with each other within uncertainty and accord with the general trend of increasing pressure and temperature outward from the "Hastings Metamorphic Low" (Fig. 1b; Carmichael *et al.*, 1978). We considered whether the predicted P–T conditions of 620–675°C and 6.5–7.5 kbar are reasonable estimates for kyanite and lower sillimanite zone conditions. Two bounding limits are the relatively lower temperature chlorite-out reaction, and the relatively higher temperature muscovite-out reaction between which the P–T conditions must lie. Experiments and thermodynamic predictions have independently constrained the chlorite-out reaction to 550–600°C at 5–10 kbar (Pattison, 2001), whereas experiments and thermodynamic predictions have independently constrained the muscovite-out reaction to 680–760°C at 5 kbar (Chatterjee & Johannes, 1974; Vielzeuf & Holloway, 1988; White *et al.*, 2001). Our predicted P–T conditions lie between 6.5 and 7.5 kbar, and at similar conditions to kyanite- and sillimanite-bearing assemblages on phase diagrams calculated for average metapelites by White *et al.* (2014b), who used thermodynamic data set 6.2 (Holland & Powell, 2011), and Pattison *et al.* (2011), who used thermodynamic data set 5.5 (Holland & Powell, 1998). An uncertainty in the above comparison is the possibility of non-equilibrium development of some mineral assemblages, especially those involving staurolite and kyanite (Pattison & Spear, 2018), which could imply lower pressures for Barrovian assemblages than predicted by current phase equilibrium modelling.

On the other hand, the order of samples, in terms of increasing temperature predicted by the modelling, does not simply match the order of the samples on the ground (Figs. 1c and 11). First, the mineral assemblages observed in kyanite zone samples K4 and C1 are predicted to be stable above 655°C, overlapping with the P–T conditions for samples from the lower sillimanite zone (Fig. 12). For staurolite–kyanite-bearing sample K4, this may be because on textural grounds kyanite did not form from reaction of staurolite as predicted in the phase diagram, but instead formed from the metastable reaction of Ms + Chl + Qz (Pattison & Spear, 2018). Another possible explanation is that the staurolite- and kyanite-forming reactions occurred at lower pressures and temperatures because of a reduced activity of H_2O. Second, the Crd–St–Oam–Grt-bearing sample C3 observed in kyanite zone occurs at lower pressure (4.5–6 kbar) than any other sample, perhaps due to the unusually low-pressure stability range of cordierite–muscovite assemblages in data set 6.2 (Pattison & Goldsmith, 2022).

The least satisfactory aspect of the thermodynamic modelling is related to the mismatch between predicted and observed mineral compositions (Fig. 13 and above discussion; see also Waters, 2019). Whereas the poor prediction of mineral compositions could be viewed an acceptable discrepancy when the mineral assemblage fields and mineral modes are satisfactorily predicted, mineral compositions exert a strong control on both. Studies in metabasites have shown that discrepancies between predicted and observed amphibole compositions lead to displaced mineral assemblage stability fields on P–T diagrams (Forshaw *et al.*, 2019; Starr *et al.*, 2020). Therefore, if mineral compositions were more closely matched for metapelites from Whetstone Lake, there could be changes to the stability fields of the predicted mineral assemblages on the P–T phase diagrams, and in turn

the P–T estimates. An important consideration in the above analysis is the uncertainty associated with the predicted mineral compositions and modal abundances. Assigning uncertainties to the thermodynamic data set and solution models, and in turn the predicted mineral compositions and modal abundances, has been discussed in several studies (Powell & Holland, 2008, 1988; Lanari & Duesterhoeft, 2019; Waters, 2019). The conclusion is that assigning uncertainties is difficult to do in a statistically rigorous yet meaningful way, and the uncertainties vary from assemblage to assemblage. Examination of the causes of the mineral compositional discrepancies, in particular an assessment of the thermodynamic parameters of mineral end members and solution models, would be a worthy follow-up to this study. We hope that when the next iteration of thermodynamic database refinement occurs, the diverse bulk compositions, mineral assemblages, modes, and compositions of Whetstone Lake will be an excellent test suite for assessing the success of the modelling.

CONCLUSIONS

We have documented an exceptional diversity of metapelitic mineral assemblages from the kyanite and lower sillimanite zones of the Whetstone Lake area, southeastern Ontario. Using a data set of petrographic observations, phase proportions, whole-rock analyses, and mineral compositions, we have demonstrated the importance of bulk composition on mineral assemblage development in an area over which there is a limited range in metamorphic grade. Our observations were compared to the predictions of phase equilibrium modelling using data set 6.2 (Holland & Powell, 2011) and the solution models of White *et al.* (2014a, 2014b), the only combination of thermodynamic data set and solution models with enough Fe^{3+}-bearing mineral end members to model the natural assemblages at Whetstone Lake. Phase diagrams were constructed for two sets of bulk compositions for each rock: one from XRF and one from combining modal abundances with representative mineral compositions. These were used to assess how sensitive the predicted mineral assemblages, proportions, and compositions are to different estimates of the reactive bulk composition. Local bulk compositions were carefully considered so as not to include portions of the rock that are unlikely to have interacted chemically at peak conditions (e.g. interiors of porphyroblasts). The quality of fit between predicted and observed values was assessed quantitatively using quality factors (Q_{asm}, Q_{vol}, and Q_{cmp}; Duesterhoeft & Lanari, 2020), augmented by a mineral-by-mineral comparison of predicted versus observed cations per formula unit.

The main conclusions of this work are:

- The differences in bulk composition in metapelites from the kyanite and sillimanite zones of the Whetstone Lake area exert a primary control on their mineral assemblages, proportions, and compositions and account for their diversity in an area where there is only a modest difference in metamorphic grade.
- Whole-rock X_{Mg}^* and $X_{Fe^{3+}}$ are the two most important compositional parameters that influence the different mineral assemblages and compositions.
- The samples additionally show a wide range of K_2O, Al_2O_3, and MnO contents that exert a secondary influence on mineral assemblages and compositions.
- Phase equilibrium modelling using either whole-rock or local bulk compositions broadly predicted a mineral assemblage field matching that observed for a wide range of bulk compositions (Q_{asm} = 100% for 12 out of 16 diagrams).

- The predicted P–T conditions of mineral assemblage fields overlap between 620–675°C and 6.5–7.5 kbar using either the whole-rock or local bulk composition, consistent with the relatively limited range of metamorphic grade represented by the sample suite.
- The match of predicted and observed mineral modes, as measured by Q_{vol}, is always better for our considered local bulk compositions than whole-rock bulk compositions, with $Q_{vol} > 90\%$ for all local bulk compositions apart from sample C1 where the assemblage was poorly predicted.
- The match of predicted and observed mineral compositions, as measured by Q_{cmp}, ranges from 20–61%, demonstrating significant discrepancies. The main mismatches include: overestimation of X^*_{Mg} in garnet, staurolite, and cordierite, overestimation of Ti in staurolite and biotite, underestimation of Si in biotite, and overestimation of Al and underestimation of Fe^{3+}, Fe^{2+}, and Mg in muscovite.

Acknowledgements

Funding

Data Availability

The data underlying this article are available in the article and in its online supplementary material.

Supplementary Data

Supplementary data are available at Journal of Petrology online.

References

Anovitz, L. M. & Essene, E. J. (1990). Thermobarometry and pressure-temperature paths in the Grenville province of Ontario. *Journal of Petrology* **31**, 197–241. https://doi.org/10.1093/petrology/31.1.197.

Armstrong, J. T. (1988). Quantitative analysis of silicate and oxide materials: comparison of Monte Carlo, ZAF, and $\varphi(\rho z)$ procedures. *Microbeam Analysis* **8**, 239–246.

Atherton, M. P. (1977). The metamorphism of the Dalradian rocks of Scotland. *Scottish Journal of Geology* **13**, 331–370. https://doi.org/10.1144/sjg13040331.

Atherton, M. P. & Brotherton, M. S. (1972). The composition of some kyanite-bearing regionally metamorphosed rocks from the Dalradian. *Scottish Journal of Geology* **8**, 203–213. https://doi.org/10.1144/sjg08030203.

Atherton, M. P. & Brotherton, M. S. (1982). Major element composition of the pelites of the Scottish Dalradian. *Geological Journal* **17**, 185–221. https://doi.org/10.1002/gj.3350170303.

Atherton, M. P. & Edmunds, W. M. (1966). An electron microprobe study of some zoned garnets from metamorphic rocks. *Earth and Planetary Science Letters* **1**, 185–193. https://doi.org/10.1016/0012-821X(66)90066-5.

Barrow, G. (1893). On an intrusion of muscovite-biotite gneiss in the south-eastern highlands of Scotland, and its accompanying metamorphism. *Quarterly Journal of the Geological Society* **49**, 330–358. https://doi.org/10.1144/GSL.JGS.1893.049.01-04.52.

Barrow, G. (1912). On the geology of lower dee-side and the southern highland border. *Proceedings of the Geologists' Association* **23**, 274–290. https://doi.org/10.1016/S0016-7878(12)80018-6.

Barth, T. F. W. (1936). Structural and petrologic studies in Dutchess County, New York: part II. Petrology and metamorphism of the Paleozoic rocks. *Bulletin of the Geological Society of America* **47**, 775–850. https://doi.org/doi:10.1130/GSAB-47-775.

Berman, R. G. (1988). Internally-consistent thermodynamic data for minerals in the system Na2O–K2O–CaO–MgO–FeO–Fe2O3–Al2O3–SiO2–TiO2–H2O–CO2. *Journal of Petrology* **29**, 445–522. https://doi.org/doi:10.1093/petrology/29.2.445.

de Béthune, P., Laduron, D. & Bocquet, J. (1975). Diffusion processes in resorbed garnets. *Contributions to Mineralogy and Petrology* **50**, 197–204. https://doi.org/10.1007/BF00371039.

Boger, S. D., White, R. W. & Schulte, B. (2012). The importance of iron speciation (Fe^{+2}/Fe^{+3}) in determining mineral assemblages: an example from the high-grade aluminous metapelites of south-eastern Madagascar. *Journal of Metamorphic Geology* **30**, 997–1018. https://doi.org/10.1111/jmg.12001.

Caddick, M. J., Konopásek, J. & Thompson, A. B. (2010). Preservation of garnet growth zoning and the duration of prograde metamorphism. *Journal of Petrology* **51**, 2327–2347. https://doi.org/10.1093/petrology/egq059.

de Capitani, C. & Brown, T. H. (1987). The computation of chemical equilibrium in complex systems containing non-ideal solutions. *Geochimica et Cosmochimica Acta* **51**, 2639–2652. https://doi.org/10.1016/0016-7037(87)90145-1.

de Capitani, C. & Petrakakis, K. (2010). The computation of equilibrium assemblage diagrams with Theriak/Domino software. *American Mineralogist* **95**, 1006–1016. https://doi.org/10.2138/am.2010.3354.

Carlson, W. D., Pattison, D. R. M. & Caddick, M. J. (2015). Beyond the equilibrium paradigm: how consideration of kinetics enhances metamorphic interpretation. *American Mineralogist* **100**, 1659–1667. https://doi.org/10.2138/am-2015-5097.

Carmichael, D. M. (1967) *Structure and progressive metamorphism in the Whetstone Lake area, Ontario with emphasis on the mechanism of prograde metamorphic reactions.* Doctoral thesis, University of California, Berkeley.

Carmichael, D. M. (1970). Intersecting Isograds in Whetstone Lake Area, Ontario. *Journal of Petrology* **11**, 147–181. https://doi.org/10.1093/petrology/11.1.147.

Carmichael, D. M. (1978). Metamorphic Bathzones and Bathograds: a measure of the depth of post-metamorphic uplift and erosion on the regional scale. *American Journal of Science* **278**, 769–797. https://doi.org/10.2475/ajs.278.6.769.

Carmichael, D. M., Moore, J. M. & Skippen, G. B. (1978) Isograds around the Hastings metamorphic "low,". In: Mackasey A. L. & Currie W. O. (eds) *Toronto '78 Field Trips Guidebook - Geological Association of Canada–Geological Association of America Combined Meeting*, pp. 325–346.

Carson, C. J., Powell, R. & Clarke, G. L. (1999). Calculated mineral equilibria for eclogites in CaO–Na$_2$O–FeO–MgO–Al$_2$O$_3$–SiO$_2$–H$_2$O: application to the Pouébo Terrane, Pam Peninsula, New Caledonia. *Journal of Metamorphic Geology* **17**, 9–24. https://doi.org/10.1046/j.1525-1314.1999.00177.x.

Cesare, B. (1999). Multi-stage pseudomorphic replacement of garnet during polymetamorphism: 2. Algebraic analysis of mineral assemblages. *Journal of Metamorphic Geology* **17**, 735–746. https://doi.org/10.1046/j.1525-1314.1999.00230.x.

Chatterjee, N. D. & Johannes, W. (1974). Thermal stability and standard thermodynamic properties of synthetic 2M1-muscovite, KAl2[AlSi3O10(OH)2]. *Contributions to Mineralogy and Petrology* **48**, 89–114. https://doi.org/10.1007/BF00418612.

Chesworth, W. (1971). Metamorphic facies series in the Grenville Province of Ontario. *Tectonophysics* **14**, 71–78. https://doi.org/10.1016/0040-1951(72)90006-6.

Chinner, G. A. (1960). Pelitic gneisses with varying ferrous/ferric ratios from Glen Clova, Angus, Scotland. *Journal of Petrology* **1**, 178–217. https://doi.org/10.1093/petrology/1.1.178.

Chinner, G. A. (1965). The kyanite isograd in Glen Clova, Angus, Scotland. *Mineralogical Magazine* **34**, 132–143. https://doi.org/10.1180/minmag.1965.034.268.11.

Connolly, J. A. D. & Cesare, B. (1993). C–O–H–S fluid composition and oxygen fugacity in graphitic metapelites. *Journal of Metamorphic Geology* **11**, 379–388. https://doi.org/10.1111/j.1525-1314.1993.tb00155.x.

Connolly, J. A. D. & Galvez, M. E. (2018). Electrolytic fluid speciation by Gibbs energy minimization and implications for subduction zone mass transfer. *Earth and Planetary Science Letters* **501**, 90–102. https://doi.org/10.1016/j.epsl.2018.08.024.

Cosca, M. A., Essene, E. J., Kunk, M. J. & Sutter, J. F. (1992). Differential unroofing within the central metasedimentary belt of the Grenville Orogen: constraints from 40Ar/39Ar thermochronology. *Contributions to Mineralogy and Petrology* **110**, 211–225. https://doi.org/10.1007/BF00310739.

Crameri, F., 2021. Scientific colour maps. https://doi.org/10.5281/zenodo.4491293.

Deer, W. A., Howie, R. A. & Zussman, J. (2013) *An introduction to the rock-forming minerals*, 3rd edn. Longman, London: Longman Group Limited. https://doi.org/10.1180/DHZ.

Dempster, T. J., La Piazza, J., Taylor, A. G., Beaudoin, N. & Chung, P. (2017). Chemical and textural equilibration of garnet during amphibolite facies metamorphism: the influence of coupled dissolution–reprecipitation. *Journal of Metamorphic Geology* **35**, 1111–1130. https://doi.org/10.1111/jmg.12278.

Dempster, T. J., Gilmour, M. I. & Chung, P. (2019). The partial equilibration of garnet porphyroblasts in pelitic schists and its control on prograde metamorphism, Glen Roy, Scotland. *Journal of Metamorphic Geology* **37**, 383–399. https://doi.org/10.1111/jmg.12467.

Diener, J. F. A. & Powell, R. (2010). Influence of ferric iron on the stability of mineral assemblages. *Journal of Metamorphic Geology* **28**, 599–613. https://doi.org/10.1111/j.1525-1314.2010.00880.x.

Dolejš, D. (2013). Thermodynamics of aqueous species at high temperatures and pressures: equations of state and transport theory. *Thermodynamics of Geothermal Fluids* **76**, 35–79. https://doi.org/10.2138/rmg.2013.76.3.

Droop, G. T. R. (1987). A general equation for estimating Fe^{3+} concentrations in ferromagnesian silicates and oxides from microprobe analyses, using stoichiometric criteria. *Mineralogical Magazine* **51**, 431–435. https://doi.org/10.1180/minmag.1987.051.361.10.

Dubacq, B., Bickle, M. J. & Evans, K. A. (2013). An activity model for phase equilibria in the H$_2$O–CO$_2$–NaCl system. *Geochimica et Cosmochimica Acta* **110**, 229–252. https://doi.org/10.1016/j.gca.2013.02.008.

Duesterhoeft, E. & Lanari, P. (2020). Iterative thermodynamic modelling—part 1: a theoretical scoring technique and a computer program (Bingo-Antidote). *Journal of Metamorphic Geology* **38**, 527–551. https://doi.org/10.1111/jmg.12538.

Duesterhoeft, E., Raase, P., Duguet, M. & Easton, R. M. (2021). The role of excess oxygen for modeling high-Mn, low-Ca garnets in metapelites from the northern central Metasedimentary Belt of the Grenville Province, Ontario, Canada. *Canadian Journal of Earth Sciences* **58**, 21–37. https://doi.org/10.1139/cjes-2019-0238.

Dunn, S. R., Markley, M. J., Kotikian, M., Achenbach, K., Montanye, B. & Peack, W. H. (2019). Geothermometry of the Western half of the central Metasedimentary Belt, Grenville Province, Ontario, and its implications. *American Mineralogist* **104**, 791–809. https://doi.org/10.2138/am-2019-6757.

Dyar, M. D., Lowe, E. W., Guidotti, C. V. & Delaney, J. S. (2002). Fe^{3+} and Fe^{2+} partitioning among silicates in metapelites: a synchrotron micro-XANES study. *American Mineralogist* **87**, 514–522. https://doi.org/10.2138/am-2002-0414.

Dyar, M. D., Breves, E. A., Emerson, E., Bell, S. W., Nelms, M., Ozanne, M.v., Peel, S. E., Carmosino, M. L., Tucker, J. M., Gunter, M. E., Delaney, J. S., Lanzirotti, A. & Woodland, A. B. (2012). Accurate determination of ferric iron in garnets by bulk Mössbauer spectroscopy and synchrotron micro-XANES. *American Mineralogist* **97**, 1726–1740. https://doi.org/10.2138/am.2012.4107.

Easton, R. M. (1992) The Grenville Province and the Proterozoic history of central and southern Ontario. In: Thurston P. C., Williams H. R., Sutcliffe R. H. & Stott G. M. (eds) *Geology of Ontario, Ontario Geological Survey, Special Volume 4, Part 2. Ontario Geological Survey*, pp.714–904.

Eskola, P. (1914) *On the petrology of the Orijärvi region in southwestern Finland Vol. 40*. Printing-office of the imperial Senate.

Eskola, P. (1915). Om sambandet mellan kemisk och mineralogisk sammansättning hos Orijärvitraktens metamorfa bergarter; on the relation between the chemical and mineralogical composition in the metamorphic rocks of the Orijärvi region. *Bulletin de la Commission Geologique de Finlande* **44**, 1–145.

Eugster, H. P. (1972) Reduction and Oxidation in Metamorphism (II). In: *24th International Geological Congress Section 10*. Montreal, pp. 3–11.

Evans, T. P. (2004). A method for calculating effective bulk composition modification due to crystal fractionation in garnet-bearing schist: implications for isopleth thermobarometry. *Journal of Metamorphic Geology* **22**, 547–557. https://doi.org/10.1111/j.1525-1314.2004.00532.x.

Evans, K. A. (2006). Redox decoupling and redox budgets: conceptual tools for the study of earth systems. *Geology* **34**, 489–492. https://doi.org/10.1130/G22390.1.

Evans, K. A. & Tomkins, A. G. (2020). Metamorphic fluids in orogenic settings. *Elements* **16**, 381–387. https://doi.org/10.2138/GSELEMENTS.16.6.381.

Evans, K. A., Powell, R. & Holland, T. J. B. (2010). Internally consistent data for Sulphur-bearing phases and application to the construction of pseudosections for mafic greenschist facies rocks in Na_2O–CaO–K_2O–FeO–MgO–Al_2O_3–SiO_2–CO_2–O–S–H_2O. *Journal of Metamorphic Geology* **28**, 667–687. https://doi.org/10.1111/j.1525-1314.2010.00890.x.

Ferry, J. M. & Burt, D. M. (1982). Characterization of metamorphic fluid composition through mineral equilibria. *Reviews in Mineralogy and Geochemistry* **10**, 207–262. https://doi.org/10.1515/9781501508172-010.

Fitton, J. G. & Gill, R. C. O. (1970). The oxidation of ferrous iron in rocks during mechanical grinding. *Geochimica et Cosmochimica Acta* **34**, 518–524. https://doi.org/10.1016/0016-7037(70)90143-2.

Ford, F. D. (2002) *Progressive Metamorphism of Flinton Group Pelitic Schists Grenville Province, Southeastern Ontario.* Doctoral thesis, Carleton University.

Forshaw, J. B. (2021) *Bulk compositional control on the metamorphism of pelitic rocks with an emphasis on the Whetstone Lake area, Southeastern Ontario.* Doctoral thesis, University of Calgary.

Forshaw, J. B. & Pattison, D. R. M. (2021). Ferrous/ferric (Fe^{2+}/Fe^{3+}) partitioning among silicates in metapelites. *Contributions to Mineralogy and Petrology* **176**, 1–26. https://doi.org/10.1007/s00410-021-01814-4.

Forshaw, J. B. & Pattison, D. R. M. (2023). Major-element geochemistry of pelites. *Geology* **51**, 39–43. https://doi.org/10.1130/G50542.1.

Forshaw, J. B., Waters, D. J., Pattison, D. R. M., Palin, R. M. & Gopon, P. (2019). A comparison of observed and thermodynamically predicted phase equilibria and mineral compositions in mafic granulites. *Journal of Metamorphic Geology* **37**, 153–179. https://doi.org/10.1111/jmg.12454.

Frost, R. B. (1991). Introduction to oxygen fugacity and its petrologic importance. *Reviews in Mineralogy and Geochemistry* **25**, 1–9. https://doi.org/10.1515/9781501508684-004.

Gaidies, F., Abart, R., De Capitani, C., Schuster, R., Connolly, J. A. D. & Reusser, E. (2006). Characterization of polymetamorphism in the Austroalpine basement east of the Tauern Window using garnet isopleth thermobarometry. *Journal of Metamorphic Geology* **24**, 451–475. https://doi.org/10.1111/j.1525-1314.2006.00648.x.

Gaidies, F., Capitani, C. & Abart, R. (2008a). THERIA-G: a software program to numerically model prograde garnet growth. *Contributions to Mineralogy and Petrology* **155**, 657–671. https://doi.org/10.1007/s00410-007-0263-z.

Gaidies, F., Capitani, C., Abart, R. & Schuster, R. (2008b). Prograde garnet growth along complex P–T–t paths: results from numerical experiments on polyphase garnet from the Wölz Complex (Austroalpine basement). *Contributions to Mineralogy and Petrology* **155**, 673–688. https://doi.org/10.1007/s00410-007-0264-y.

Galvez, M. E., Manning, C. E., Connolly, J. A. D. & Rumble, D. (2015). The solubility of rocks in metamorphic fluids: a model for rock-dominated conditions to upper mantle pressure and temperature. *Earth and Planetary Science Letters* **430**, 486–498. https://doi.org/10.1016/j.epsl.2015.06.019.

Ganguly, J. (1972). Staurolite stability and related parageneses: theory, experiments, and applications. *Journal of Petrology* **13**, 335–365. https://doi.org/10.1093/petrology/13.2.335.

García-Arias, M. (2020). Consistency of the activity–composition models of Holland, Green, and Powell (2018) with experiments on natural and synthetic compositions: a comparative study. *Journal of Metamorphic Geology* **38**, 993–1010. https://doi.org/10.1111/jmg.12557.

Geiger, C. A., Rager, H. & Czank, M. (2000). Cordierite III: the site occupation and concentration of Fe^{3+}. *Contributions to Mineralogy and Petrology* **140**, 344–352. https://doi.org/10.1007/s004100000194.

George, F. R., Waters, D. J., Gough, S. J., Searle, M. P. & Forshaw, J. B. (2022). Phase equilibria and microstructural constraints on the high temperature building of the Kohistan island arc: the Jijal garnet granulites, northern Pakistan. *Journal of Metamorphic Geology* **40**, 145–174. https://doi.org/10.1111/jmg.12622.

Gervais, F. & Trapy, P. H. (2021). Testing solution models for phase equilibrium (forward) modeling of partial melting experiments. *Contributions to Mineralogy and Petrology* **176**, 1–18. https://doi.org/10.1007/s00410-020-01762-5.

Goldschmidt, V. M. (1911). Die Kontaktmetamorphose im Kristianiagebiet. *In kommission bei J. Dybwad* **34**, 812–819. https://doi.org/10.1080/11035891209446981.

Gopon, P., Forshaw, J. B., Wade, J., Waters, D. J. & Gopon, C. (2022). Seeing through metamorphic overprints in Archean granulites: combined high resolution thermometry and phase equilibrium modeling of the Lewisian complex, Scotland. *American Mineralogist* **107**, 1487–1500. https://doi.org/10.2138/am-2022-8214ccby.

Grey, I. E. & Reid, A. F. (1975). The structure of Pseudorutile and its role in the natural alteration of llmenite. *American Mineralogist* **60**, 898–906.

Guevara, V. E. & Caddick, M. J. (2016). Shooting at a moving target: phase equilibria modelling of high-temperature metamorphism. *Journal of Metamorphic Geology* **34**, 209–235. https://doi.org/10.1111/jmg.12179.

Guidotti, C. V. (1974). Transition from staurolite to sillimanite zone, Rangeley quadrangle, Maine. *Bulletin of the Geological Society of America* **85**, 475–490. https://doi.org/10.1130/0016-7606(1974)85<475:TFSTSZ>2.0.CO;2.

Guidotti, C. V., Cheney, J. T. & Conatore, P. D. (1975). Coexisting cordierite + biotite + chlorite from the Rumford quadrangle, Maine. *Geology* **3**, 147–148. https://doi.org/10.1130/0091-7613(1975)3<147:CCBCFT>2.0.CO;2.

Guidotti, C. V., Cheney, J. T. & Guggenheim, S. (1977). Distribution of titanium between muscovite and biotite in pelitic schists coexisting Maine. *American Mineralogist* **62**, 438–448.

Hames, W. E. & Menard, T. (1993). Fluid-assisted modification of garnet composition along rims, cracks, and mineral inclusion boundaries in samples of amphibolite facies schists. *American Mineralogist* **78**, 338–344.

Harte, B. (2022) *Kyanite- and cordierite-bearing assemblages in Barrow's staurolite zone, in: MSG RiP.* University of St Andrews.

Harte, B., & Henley, K. J. (1966). Occurrence of compositionally zoned almanditic garnets in regionally metamorphosed rocks. *Nature* **210**, 689-692. https://doi.org/10.1038/210689a0.

Hawthorne, F. C., Oberti, R., Harlow, G. E., Maresch, W. V., Martin, R. F., Schumacher, J. C. & Welch, M. D. (2012). IMA report: nomenclature of the amphibole supergroup. *American Mineralogist* **97**, 2031–2048. https://doi.org/10.2138/am.2012.4276.

Helgeson, H. C. & Kirkham, D. H. (1974). Theoretical prediction of the thermodynamic behaviour of aqueous electrolytes at high pressures and temperatures: II. Debye-Huckel parameters for activity coefficients and relative partial molal properties. *American Journal of Science* **274**, 1199–1261. https://doi.org/10.2475/ajs.274.10.1199.

Helgeson, H. C. & Kirkham, D. H. (1976). Theoretical prediction of the thermodynamic behavior of aqueous electrolytes at high pressures and temperatures: III. Equation of state for aqueous species at infinite dilution. *American Journal of Science* **276**, 97–240. https://doi.org/10.2475/ajs.276.2.97.

Helgeson, H. C., Kirkham, D. H. & Flowers, G. C. (1981). Thermodynamic behavior of aqueous electrolytes at high pressures and temperatures: IV. Calculation of activity coefficients, osmotic coefficients, and apparent molal and stand and relative partial

molal properties to 600 °C and 5 kbar. *American Journal of Science* **281**, 1249–1516. https://doi.org/10.2475/ajs.281.10.1249.

Henry, D. J. & Guidotti, C. (2002). Ti in biotite from metapelitic rocks: temperature effects, crystallochemical controls and petrologic applications. *American Mineralogist* **87**, 375–382. https://doi.org/10.2138/am-2002-0401.

Henry, D. J., Guidotti, C. V. & Thomson, J. A. (2005). The Ti-saturation surface for low-to-medium pressure metapelitic biotites: implications for geothermometry and Ti-substitution mechanisms. *American Mineralogist* **90**, 316–328. https://doi.org/10.2138/am.2005.1498.

Hietanen, A. (1967). On the facies series in various types of metamorphism. *Journal of Geology* **75**, 187–214. https://doi.org/10.1086/627246.

Hillebrand, W. F. (1908). The influence of fine grinding on the water and ferrous-iron content of minerals and rocks. *Journal of the American Chemical Society* **30**, 1120–1131. https://doi.org/10.1021/ja01949a010.

Holland, T. J. B. & Powell, R. (1998). An internally consistent thermodynamic data set for phases of petrological interest. *Journal of Metamorphic Geology* **16**, 309–343. https://doi.org/10.1111/j.1525-1314.1998.00140.x.

Holland, T. J. B. & Powell, R. (2003). Activity-composition relations for phases in petrological calculations: an asymmetric multicomponent formulation. *Contributions to Mineralogy and Petrology* **145**, 492–501. https://doi.org/10.1007/s00410-003-0464-z.

Holland, T. J. B. & Powell, R. (2011). An improved and extended internally consistent thermodynamic dataset for phases of petrological interest, involving a new equation of state for solids. *Journal of Metamorphic Geology* **29**, 333–383. https://doi.org/10.1111/j.1525-1314.2010.00923.x.

Hollister, L. S. (1966). Garnet zoning: an interpretation based on the Rayleigh fractionation model. *Science* **154**, 1647-1651. https://doi.org/10.1126/science.154.3757.1647.

Hounslow, A. W. & Moore, J. M. (1967). Chemical Petrology of Grenville Schists near Fernleigh, Ontario. *Journal of Petrology* **8**, 1–28. https://doi.org/10.1093/petrology/8.1.1.

Howarth, R. J. (1998). Improved estimators of uncertainty in proportions, point-counting, and pass-fail test results. *American Journal of Science* **298**, 594–607. https://doi.org/10.2475/ajs.298.7.594.

de Hoÿm de Marien, L., le Bayon, B., Pitra, P., van den Driessche, J., Poujol, M. & Cagnard, F. (2019). Two-stage Variscan metamorphism in the Canigou massif: evidence for crustal thickening in the Pyrenees. *Journal of Metamorphic Geology*. **37**, 863–888. https://doi.org/10.1111/jmg.12487.

Hudson, N. F. C. & Harte, B. (1985). K$_2$O-poor, aluminous assemblages from the Buchan Dalradian, and the variety of orthoamphibole assemblages in aluminous bulk compositions in the amphibolite facies. *American Journal of Science* **285**, 224–266. https://doi.org/10.2475/ajs.285.3.224.

Hynes, A. & Rivers, T. (2010). Protracted continental collision—evidence from the Grenville Orogen. *Canadian Journal of Earth Sciences* **47**, 591–620. https://doi.org/10.1139/E10-003.

Kamineni, D. C. (1979). Metasedimentary cordierite-gedrite rocks of Archean age near Yellowknife, Canada. *Precambrian Research* **9**, 289–301. https://doi.org/10.1016/0301-9268(79)90008-1.

Kamineni, D. C., Stone, D. & Johnston, P. J. (1991). Metamorphism and mineral chemistry of Quetico sedimentary rocks near Atikokan, Ontario, Canada. *Neues Jahrbuch für Mineralogie - Abhandlungen* **162**, 311–337.

Kendrick, J. & Indares, A. (2018). The reaction history of kyanite in high-P aluminous granulites. *Journal of Metamorphic Geology* **36**, 125–146. https://doi.org/10.1111/jmg.12286.

Kohn, M. J. & Spear, F. (2000). Retrograde net transfer reaction insurance for pressure-temperature estimates. *Geology* **28**, 1127–1130. https://doi.org/10.1130/0091-7613(2000)028<1127:RNTRIF>2.3.CO;2.

Laakso, R. K. (1968) *Geology of Lake Township, Hastings County*, No. 54. Ontario Department of Mines.

Labotka, T. C. (1980). Petrology of a medium-pressure regional metamorphic terrane, Funeral Mountains, California. *American Mineralogist* **65**, 670–689.

Labotka, T. C. (1981). Petrology of an andalusite-type regional metamorphic terrane, Panamint mountains, California. *Journal of Petrology* **22**, 261–296. https://doi.org/10.1093/petrology/22.2.261.

Lal, R. K., & Moorhouse, W. W. (1969). Cordierite–gedrite rocks and associated gneisses of Fishtail Lake, Harcourt Township, Ontario. *Canadian Journal of Earth Sciences* **6**, 145-165. https://doi.org/10.1139/e69-014.

Lal, R. K. & Shukla, R. S. (1975). Low-pressure regional metamorphism in the northern portion of the Khetri Copper Belt of Rajasthan, India. *Neues Jahrbuch für Mineralogie - Abhandlungen* **124**, 294–325.

Lanari, P. & Duesterhoeft, E. (2019). Modeling metamorphic rocks using equilibrium thermodynamics and internally consistent databases: past achievements, problems and perspectives. *Journal of Petrology* **60**, 19–56. https://doi.org/10.1093/petrology/egy105.

Lanari, P. & Engi, M. (2017). Local bulk composition effects on metamorphic mineral assemblages. *Reviews in Mineralogy and Geochemistry* **83**, 55–102. https://doi.org/10.2138/rmg.2017.83.3.

Lanari, P. & Hermann, J. (2021). Iterative thermodynamic modelling—part 2: tracing equilibrium relationships between minerals in metamorphic rocks. *Journal of Metamorphic Geology* **39**, 651–674. https://doi.org/10.1111/jmg.12575.

Lanari, P., Vidal, O., De Andrade, V., Dubacq, B., Lewin, E., Grosch, E. G. & Schwartz, S. (2014). XMapTools: a MATLAB©-based program for electron microprobe X-ray image processing and geothermobarometry. *Computational Geosciences* **62**, 227–240. https://doi.org/10.1016/j.cageo.2013.08.010.

Lanari, P., Giuntoli, F., Loury, C., Burn, M. & Engi, M. (2017). An inverse modeling approach to obtain P–T conditions of metamorphic stages involving garnet growth and resorption. *European Journal of Mineralogy* **29**, 181–199. https://doi.org/10.1127/ejm/2017/0029-2597.

Lanari, P., Vho, A., Bovay, T., Airaghi, L. & Centrella, S. (2019). Quantitative compositional mapping of mineral phases by electron probe micro-analyser. *Geological Society - Special Publications* **478**, 39–63. https://doi.org/10.1144/SP478.4.

Lang, H. M. (1991). Quantitative interpretation of within-outcrop variation in metamorphic assemblage in staurolite–kyanite–grade metapelites, Baltimore, Maryland. *The Canadian Mineralogist* **29**, 655–671.

Lang, H. M. & Rice, J. M. (1985). Regression modelling of metamorphic reactions in metapelites, snow peak, northern Idaho. *Journal of Petrology* **26**, 857–887. https://doi.org/10.1093/petrology/26.4.857.

lo Pò, D. & Braga, R. (2014). Influence of ferric iron on phase equilibria in greenschist facies assemblages: the hematite-rich metasedimentary rocks from the Monti Pisani (Northern Apennines). *Journal of Metamorphic Geology* **32**, 371–387. https://doi.org/10.1111/jmg.12076.

Lumbers, S.B., Vertolli, V.M., 2000a. Precambrian geology, Bannockburn area, Preliminary Map, scale 1:50 000.

Lumbers, S.B., Vertolli, V.M., 2000b. Precambrian geology, Coe Hill area, Preliminary Map, scale 1:50 000.

Lumbers, S. B., Heaman, L. M., Vertolli, V. M., Wu, T. W., Gower, C. F., Rivers, T. & Ryan, A. B. (1990) Nature and timing of Middle Proterozoic magmatism in the Central Metasedimentary Belt,

Grenville Province, Ontario. Mid-Proterozoic Laurentia–Baltica. In: Gower C. F., Rivers T. & Ryan A. B. (eds) *Geological Association of Canada, Special Paper 38*, pp.243–276.

Manning, C. E. (2018). Fluids of the lower crust: deep is different. *Annual Review of Earth and Planetary Sciences* **46**, 67–97. https://doi.org/10.1146/annurev-earth-060614-105224.

Markley, M. J., Dunn, S. R., Jercinovic, M. J., Peck, W. H. & Williams, M. L. (2018). Monazite U–Th–Pb geochronology of the central Metasedimentary Belt boundary zone (CMBbz), Grenville Province, Ontario Canada. *Canadian Journal of Earth Sciences* **55**, 1063–1078. https://doi.org/10.1139/cjes-2018-0039.

Marmo, B. A., Clarke, G. L. & Powell, R. (2002). Fractionation of bulk rock composition due to porphyroblast growth: effects on eclogite facies mineral equilibria, Pam Peninsula, New Caledonia. *Journal of Metamorphic Geology* **20**, 151–165. https://doi.org/10.1046/j.0263-4929.2001.00346.x.

Martin, L. A. J. J., Ballèvre, M., Boulvais, P., Halfpenny, A., Vanderhaeghe, O., Duchêne, S. & Deloule, E. (2011). Garnet re-equilibration by coupled dissolution–reprecipitation: evidence from textural, major element and oxygen isotope zoning of "cloudy" garnet. *Journal of Metamorphic Geology* **29**, 213–231. https://doi.org/10.1111/j.1525-1314.2010.00912.x.

McCarron, T. J. A., Gaidies, F., McFarlane, C. R. M., Easton, R. M. & Jones, P. (2014). Coupling thermodynamic modeling and high-resolution in situ LA–ICP–MS monazite geochronology: evidence for Barrovian metamorphism late in the Grenvillian history of southeastern Ontario. *Mineralogy and Petrology* **108**, 741–758. https://doi.org/10.1007/s00710-014-0343-5.

McLellan, E. (1985). Metamorphic reactions in the kyanite and sillimanite zones of the barrovian type area. *Journal of Petrology* **26**, 789–818. https://doi.org/10.1093/petrology/26.4.789.

Mezger, K., Essene, E. J., van der Pluijm, B. A. & Halliday, A. N. (1993). U-Pb geochronology of the Grenville Orogen of Ontario and New York: constraints on ancient crustal tectonics. *Contributions to Mineralogy and Petrology* **114**, 13–26. https://doi.org/10.1007/BF00307862.

Miron, G. D., Wagner, T., Kulik, D. A. & Lothenbach, B. (2017). An internally consistent thermodynamic dataset for aqueous species in the system Ca–Mg–Na–K–Al–Si–O–H–C–Cl to 800 °C and 5 kbar. *American Journal of Science* **317**, 755–806. https://doi.org/10.2475/07.2017.01.

Miyashiro, A. (1961). Evolution of metamorphic belts. *Journal of Petrology* **2**, 277–311. https://doi.org/10.1093/petrology/2.3.277.

Moore, J. M. & Waters, D. J. (1990). Geochemistry and origin of cordierite-orthoamphibole/orthopyroxene-phlogopite rocks from Namaqualand, South Africa. *Chemical Geology* **85**, 77–100. https://doi.org/10.1016/0009-2541(90)90124-P.

Moss, B. E., Haskin, L. A. & Dymek, R. F. (1996). Compositional variations in metamorphosed sediments of the Littleton Formation, New Hampshire, and the Carrabassett Formation, Maine, at sub-hand specimen, outcrop, and regional scales. *American Journal of Science* **296**, 473–505. https://doi.org/10.2475/ajs.296.5.473.

Moynihan, D. P. & Pattison, D. R. M. (2013). An automated method for the calculation of P–T paths from garnet zoning, with application to metapelitic schist from the Kootenay arc, British Columbia, Canada. *Journal of Metamorphic Geology* **31**, 525–548. https://doi.org/10.1111/jmg.12032.

Mücke, A. & Chaudhuri, J. N. B. (1991). The continuous alteration of ilmenite through pseudorutile to leucoxene. *Ore Geology Reviews* **6**, 25–44. https://doi.org/10.1016/0169-1368(91)90030-B.

Munksgaard, N. C. (1988). Source of the Cooma Granodiorite, New South Wales—a possible role of fluid–rock interactions.

Australian Journal of Earth Sciences **35**, 363–377. https://doi.org/10.1080/08120098808729454.

Palin, R. M., Weller, O. M., Waters, D. J. & Dyck, B. (2016). Quantifying geological uncertainty in metamorphic phase equilibria modelling; a Monte Carlo assessment and implications for tectonic interpretations. *Geoscience Frontiers* **7**, 591–607. https://doi.org/10.1016/j.gsf.2015.08.005.

Pattison, D. R. M. (1987). Variations in Mg/(Mg + Fe), F, and (Fe, Mg)Si = 2Al in pelitic minerals in the Ballachulish thermal aureole, Scotland. *American Mineralogist* **72**, 255–272.

Pattison, D. R. M. (2001). Instability of Al_2SiO_5 "triple-point" assemblages in muscovite+biotite+quartz-bearing metapelites, with implications. *American Mineralogist* **86**, 1414–1422. https://doi.org/10.2138/am-2001-11-1210.

Pattison, D. R. M. & Debuhr, C. L. (2015). Petrology of metapelites in the Bugaboo aureole, British Columbia, Canada. *Journal of Metamorphic Geology* **33**, 437–462. https://doi.org/10.1111/jmg.12128.

Pattison, D. R. M. & Goldsmith, S. A. (2022). Metamorphism of the Buchan-type area, NE Scotland, and its relation to the adjacent Barrovian domain. *Journal of the Geological Society of London* **179**, 1–33. https://doi.org/10.1144/jgs2021-040.

Pattison, D. R. M. & Spear, F. S. (2018). Kinetic control of staurolite–Al_2SiO_5 mineral assemblages: implications for Barrovian and Buchan metamorphism. *Journal of Metamorphic Geology* **36**, 667–690. https://doi.org/10.1111/jmg.12302.

Pattison, D. R. M. & Tinkham, D. K. (2009). Interplay between equilibrium and kinetics in prograde metamorphism of pelites: an example from the Nelson aureole, British Columbia. *Journal of Metamorphic Geology* **27**, 249–279. https://doi.org/10.1111/j.1525-1314.2009.00816.x.

Pattison, D. R. M. & Tracy, R. J. (1991) Phase equilibria and thermobarometry of metapelites. In: *Contact Metamorphism: Reviews in Mineralogy and Geochemistry 26*. Mineralogical Society of America, pp.105–206. https://doi.org/10.1515/9781501509612-007.

Pattison, D. R. M. & Vogl, J. J. (2005). Contrasting sequences of metapelitic mineral-assemblages in the aureole of the tilted Nelson Batholith, British Columbia: implications for phase equilibria and pressure determination in andalusite–sillimanite-type settings. *The Canadian Mineralogist* **43**, 51–88. https://doi.org/10.2113/gscanmin.43.1.51.

Pattison, D. R. M., de Capitani, C. & Gaidies, F. (2011). Petrological consequences of variations in metamorphic reaction affinity. *Journal of Metamorphic Geology* **29**, 953–977. https://doi.org/10.1111/j.1525-1314.2011.00950.x.

Pigage, L. C. (1982). Linear regression analysis of sillimanite-forming reactions at Azure Lake, British Columbia. *The Canadian Mineralogist* **20**, 349–378.

Pokrovskii, V. A. & Helgeson, H. C. (1997). Thermodynamic properties of aqueous species and the solubilities of minerals at high pressures and temperatures: the system Al_2O_3–H_2O–KOH. *Chemical Geology* **137**, 221–242. https://doi.org/10.1016/S0009-2541(96)00167-2.

Powell, R. & Holland, T. J. B. (1988). An internally consistent dataset with uncertainties and correlations: 3. Applications to geobarometry, worked examples and a computer program. *Journal of Metamorphic Geology* **6**, 173–204. https://doi.org/10.1111/j.1525-1314.1988.tb00415.x.

Powell, R. & Holland, T. J. B. (2008). On thermobarometry. *Journal of Metamorphic Geology* **26**, 155–179. https://doi.org/10.1111/j.1525-1314.2007.00756.x.

Quinn, R. J., Valley, J. W., Zeb Page, F. & Fournelle, J. H. (2016). Accurate determination of ferric iron in garnets. *American Mineralogist* **101**, 1704–1707. https://doi.org/10.2138/am-2016-5695.

Rathmell, M. A., Streepey, M. M., Essene, E. J. & van der Pluijm, B. A. (1999). Comparison of garnet–biotite, calcite–graphite, and calcite–dolomite thermometry in the Grenville Orogen; Ontario, Canada. *Contributions to Mineralogy and Petrology* **134**, 217–231. https://doi.org/10.1007/s004100050480.

Reay, A. (1981). The effect of disc mill grinding on some rock-forming minerals. *Mineralogical Magazine* **44**, 179–182. https://doi.org/10.1180/minmag.1981.044.334.10.

Ridley, J. (1985) The Effect of Reaction Enthalpy on the Progress of a Metamorphic Reaction. In: Thompson A. B. & Rubie D. C. (eds) *Advances in Physical Geochemistry*, Vol. **4**. New York, NY: Springer, pp.80–97.

Ridley, J. & Thompson, A. B. (1986) The role of mineral kinetics in the development of metamorphic microtextures. In: Walther J. V. & Wood B. J. (eds) *Fluid-rock interactions during metamorphism, Advances in Physical Geochemistry*, Vol. **5**. New York, NY: Springer, pp.154–193.

Rivers, T. (2008). Assembly and preservation of lower, mid, and upper orogenic crust in the Grenville Province—implications for the evolution of large hot long-duration orogens. *Precambrian Research* **167**, 237–259. https://doi.org/10.1016/j.precamres.2008.08.005.

Roduit, N. (2020) *JMicroVision: Image analysis toolbox for measuring and quantifying components of high-definition images*. https://jmicrovision.github.io/.

Rumble, D. (1978). Mineralogy, petrology, and oxygen isotopic geochemistry of the Clough Formation, Black Mountain, Western New Hampshire, U.S.A. *Journal of Petrology* **19**, 317–340. https://doi.org/10.1093/petrology/19.2.317.

Santos, C. A., Moraes, R. & Szabó, G. A. J. (2019). A comparison between phase diagram modelling of metamafic rocks and experimental and independent thermobarometric data. *Lithos* **340-341**, 108–123. https://doi.org/10.1016/j.lithos.2019.04.024.

Schorn, S. & Diener, J. F. A. (2019). Seemingly disparate temperatures recorded in coexisting granulite facies lithologies. *Journal of Metamorphic Geology* **37**, 1049–1078. https://doi.org/10.1111/jmg.12500.

Shaw, D. (1956). Geochemistry of pelitic rocks. Part III: major elements and general geochemistry. *Bulletin of the Geological Society of America* **67**, 919–934. https://doi.org/10.1130/0016-7606(1956)67[919:GOPRPI]2.0.CO;2.

Shock, E. L., Helgeson, H. C. & Sverjensky, D. A. (1989). Calculation of the thermodynamic and transport properties of aqueous species at high pressures and temperatures: standard partial molal properties of inorganic neutral species. *Geochimica et Cosmochimica Acta* **53**, 2157–2183. https://doi.org/10.1016/0016-7037(89)90341-4.

Shock, E. L., Oelkers, E. H., Johnson, J. W., Sverjensky, D. A. & Helgeson, H. C. (1992). Calculation of the thermodynamic properties of aqueous species at high pressures and temperatures. Effective electrostatic radii, dissociation constants and standard partial molal properties to 1000 °C and 5 kbar. *Journal of the Chemical Society, Faraday Transactions* **88**, 803–826. https://doi.org/10.1039/FT9928800803.

Spear, F. S. (1993) *Metamorphic phase equilibria and pressure-temperature-time paths*. Washington, DC: Mineralogical Society of America.

Starr, P. G., Pattison, D. R. M. & Ames, D. E. (2020). Mineral assemblages and phase equilibria of metabasites from the prehnite–pumpellyite to amphibolite facies, with the Flin Flon Greenstone Belt (Manitoba) as a type example. *Journal of Metamorphic Geology* **38**, 71–102. https://doi.org/10.1111/jmg.12513.

Streepey, M. M., Essene, E. J. & van der Pluijm, B. A. (1997). A compilation of thermobarometric data from the Metasedimentary Belt of the Grenville Province, Ontario and New York state. *The Canadian Mineralogist* **35**, 1237–1247.

Sverjensky, D. A., Shock, E. L. & Helgeson, H. C. (1997). Prediction of the thermodynamic properties of aqueous metal complexes to 1000 °C and 5 kb. *Geochimica et Cosmochimica Acta* **61**, 1359–1412. https://doi.org/10.1016/S0016-7037(97)00009-4.

Temple, A. K. (1966). Alteration of ilmenite. *Economic Geology* **61**, 695–714. https://doi.org/10.2113/gsecongeo.61.4.695.

Thompson, J. B. (1957). The graphical analysis of mineral assemblages in pelitic schists. *American Journal of Science* **42**, 842–858.

Thompson, A. B. (1976a). Mineral reactions in pelitic rocks: II. Calculation of some P–T–X(Fe–Mg) phase relations. *American Journal of Science* . https://doi.org/10.2475/ajs.276.4.425.

Thompson, A. B. (1976b). Mineral reactions in pelitic rocks: I. Prediction of P–T–X(Fe–Mg) phase relations. *American Journal of Science* . https://doi.org/10.2475/ajs.276.4.401.

Thompson, J. B., Jr. (1972) Oxides and sulfides in regional metamorphism of pelitic schists. In: *24th International Geological Congress Section 10*. Montreal, pp.27–35.

Tinkham, D. K. & Ghent, E. D. (2005). Estimating P–T conditions of garnet growth with isochemical phase-diagram sections and the problem of effective bulk-composition. *The Canadian Mineralogist* **43**, 35–50. https://doi.org/10.2113/gscanmin.43.1.35.

Vallance, T. G. (1967). Mafic rock alteration and isochemical development of some cordierite–anthophyllite rocks. *Journal of Petrology* **8**, 84–96. https://doi.org/10.1093/petrology/8.1.84.

Vidale, R. (1974) Metamorphic Differentiation Layering in Pelitic Rocks of Dutchess County. In: Hojmann A. W., Giletti B. J., Yoder H. S., Jr. & Yund R. A. (eds) *Geochemical Transport and Kinetics*. New York: Carnegie Institution of Washington, pp.273–286.

Vielzeuf, D. & Holloway, J. R. (1988). Experimental determination of the fluid-absent melting relations in the pelitic system. *Contributions to Mineralogy and Petrology* **98**, 257–276. https://doi.org/10.1007/bf00375178.

Warr, L. N. (2021). IMA–CNMNC approved mineral symbols. *Mineralogical Magazine* **85**, 291–320. https://doi.org/10.1180/mgm.2021.43.

Waters, D. J. (2019) Metamorphic constraints on the tectonic evolution of the High Himalaya in Nepal: the art of the possible. In: Treloar P. J. & Searle M. P. (eds) *Himalayan Tectonics: A Modern Synthesis*. Geological Society, LondonSpecial Publications, pp. 325–375. https://doi.org/10.1144/SP483-2018-187.

Waters, D. J. & Charnley, N. R. (2002). Local equilibrium in polymetamorphic gneiss and the titanium substitution in biotite. *American Mineralogist* **87**, 383–396. https://doi.org/10.2138/am-2002-0402.

Waters, D. J. & Lovegrove, D. P. (2002). Assessing the extent of disequilibrium and overstepping of prograde metamorphic reactions in metapelites from the Bushveld Complex aureole, South Africa. *Journal of Metamorphic Geology* **20**, 135–149. https://doi.org/10.1046/j.0263-4929.2001.00350.x.

White, R. W., Powell, R., Holland, T. J. B. & Worley, B. A. (2000). The effect of TiO_2 and Fe_2O_3 on metapelitic assemblages at greenschist and amphibolite facies conditions: mineral equilibria calculations in the system K_2O–FeO–MgO–Al_2O_3–SiO_2–H_2O–TiO_2–Fe_2O_3. *Journal of Metamorphic Geology* **18**, 497–511. https://doi.org/10.1046/j.1525-1314.2000.00269.x.

White, R. W., Powell, R. & Holland, T. J. B. (2001). Calculation of partial melting equilibria in the system Na_2O-CaO-K_2O-FeO-MgO-Al_2O_3-SiO_2-H_2O (NCKFMASH). *Journal of Metamorphic Geology* **19**, 139–153. https://doi.org/10.1046/j.0263-4929.2000.00303.x.

White, R. W., Powell, R. & Clarke, G. L. (2002). The interpretation of reaction textures in Fe-rich metapelitic granulites of the Musgrave Block, Central Australia: constraints from mineral equilibria calculations in the system. *Journal of Metamorphic Geology* **20**, 41–55. https://doi.org/10.1046/j.0263-4929.2001.00349.x.

White, R. W., Powell, R., Holland, T. J. B., Johnson, T. E. & Green, E. C. R. (2014a). New mineral activity–composition relations for thermodynamic calculations in metapelitic systems. *Journal of Metamorphic Geology* **32**, 261–286. https://doi.org/10.1111/jmg.12071.

White, R. W., Powell, R. & Johnson, T. E. (2014b). The effect of Mn on mineral stability in metapelites revisited: new a-x relations for manganese-bearing minerals. *Journal of Metamorphic Geology* **32**, 809–828. https://doi.org/10.1111/jmg.12095.

Whitney, D. L., Mechum, T. A., Dilek, Y. & Kuehner, S. M. (1996). Modification of garnet by fluid infiltration during regional metamorphism in garnet through sillimanite-zone rocks, Dutchess County, New York. *American Mineralogist* **81**, 696–705. https://doi.org/10.2138/am-1996-5-617.

Wilson, A. D. (1955). A new method for the determination of ferrous iron in rocks and minerals. *Bulletin of the Geological Survey of Great Britain* **9**, 56–58.

Wolfe, O. M., Spear, F. S. & Harrison, T. M. (2021). Pronounced and rapid exhumation of the Connecticut Valley Trough revealed through quartz in garnet Raman barometry and diffusion modelling of garnet dissolution–reprecipitation reactions. *Journal of Metamorphic Geology* **39**, 1045–1069. https://doi.org/10.1111/jmg.12601.

Yardley, B. W. D. & Bodnar, R. J. (2014). Fluids in the continental crust. *Geochemical perspectives*, **3**.

Zeh, A. (2001). Inference of a detailed P–T path from P–T pseudosections using metapelitic rocks of variable composition from a single outcrop, Shackleton Range, Antarctica. *Journal of Metamorphic Geology* **19**, 329–350. https://doi.org/10.1046/j.0263-4929.2000.00314.x.

Zou, L., Guo, J. H., Huang, G. Y., Jiao, S. J., Tian, Z. H. & Liu, P. H. (2022). The effect of bulk rock composition in phase equilibria modelling: a case study of mafic granulites from the North China Craton. *Contributions to Mineralogy and Petrology* **177**, 1–24. https://doi.org/10.1007/s00410-022-01887-9.

Zuluaga, C. A., Stowell, H. H. & Tinkham, D. K. (2005). The effect of zoned garnet on metapelite pseudosection topology and calculated metamorphic P–T paths. *American Mineralogist* **90**, 1619–1628. https://doi.org/10.2138/am.2005.1741.